Damping mechanisms of internal waves in continuously stratified rotating basins

K. SHIMIZU† AND J. IMBERGER

Centre for Water Research, University of Western Australia, Crawley, WA 6009, Australia

Damping mechanisms, damping rates and the dissipative modal structure of internal waves in stratified rotating circular basins are investigated analytically. The damping is shown to be due to a combination of the internal-wave cancelling, where waves emitted by the oscillatory boundary layers destructively interact with the parent wave and drain energy from it, and spin-down modified by the periodicity, where the energy is drained by the sinks and sources at the bottom corner caused by a discontinuity in the Ekman transport. It is shown that super-inertial Poincaré waves and sub-inertial Kelvin waves are damped predominantly by the internal-wave cancelling and modified spin-down, respectively. These processes also modify the internal-wave structure; for super-inertial waves, the boundary-layer-generated waves intensify the interior flow in the lower part of the water column and delay the phase relative to the isopycnal displacements, but for sub-inertial waves, the Ekman pumping and the corner sinks and sources add a horizontal circular flow that slants the crest and trough backwards near the wall.

1. Introduction

This study is motivated by fast damping of internal waves observed in a strongly stratified rotating lake, where the dominant basin-scale internal waves were damped within a few periods (e-folding time in terms of amplitude) (Shimizu & Imberger 2008) unlike laboratory experiments by Wake, Ivey & Imberger (2005), who reported the damping over 10–14 periods. Analysing the energy balance, bottom friction was considered as the primary cause of the damping (Shimizu & Imberger 2008). In stratified lakes, the effect of bottom friction is confined to a relatively thin, well-mixed bottom boundary layer (Wüest, Piepke & Van Senden 2000; Lemckert *et al.* 2004), and the interior remains close to laminar (Saggio & Imberger 2001); however, the momentum defect (and energy loss) occurring in the boundary layer must be transferred back into the stratified interior in which most of the momentum (and energy) is stored. Diffusion cannot transfer momentum within a time scale of a few days in a lake with a typical depth of 100 m. In this paper, we investigate damping of basin-scale internal waves by thin boundary layers; two well-known damping mechanisms are combined to understand the observed rapid damping. First, the damping mechanism investigated by Johns (1968) and Dore (1968) is relevant for relatively high-frequency basin-scale waves, and second, the well-known spin-down (Greenspan 1968; Pedlosky 1979; Gill 1982) applies to steady circulations and

† Email address for correspondence: shimizu@cwr.uwa.edu.au

low-frequency motions, such as shelf waves and Kelvin waves (Romea & Allen 1984; Mitsudera & Hanawa 1988).

These two limiting problems have already been well studied. If the wave frequency is much higher than the inertial frequency, then the basin-scale internal wave in a rotating basin degenerates into a simple internal seiche. Such waves are damped by the viscosity of the fluid acting in a thin layer underneath the surface, in the interior of the fluid and in a thin boundary layer adjacent to the solid walls of the basin; the damping rates are proportional to $\nu^{3/2}$, ν and $\nu^{1/2}$, respectively (e.g. Ursell 1952), indicating that damping due to bottom friction dominates in shallow basins (e.g. LeBlond 1966). The damping rate is most conveniently calculated by dividing the rate of energy dissipation in these thin layers by the total energy of the basin-scale seiches (e.g. Lamb 1932; Ursell 1952). However, how the energy of the basin-scale waves is actually siphoned from the waves into the thin boundary layers is rather subtle. To understand this mechanism, it is necessary to carry out a perturbation analysis assuming small viscosity as discussed by Johns (1968). Assuming progressive surface waves with the angular frequency ω, he showed that surface waves locally support, to first order, a Stokes layer at the bottom boundary. However, spatial variability of the flow causes the Stokes layer to have a variable thickness and induces a vertical velocity anomaly at the top of the bottom boundary layer, given by

$$w_E = \sqrt{\frac{\nu}{\mathrm{i}\omega}}(\boldsymbol{\nabla} \cdot \boldsymbol{v}), \qquad (1.1)$$

where w_E is the velocity anomaly normal to the boundary; $\mathrm{i} = \sqrt{-1}$ is the imaginary unit; ν is the kinematic viscosity; $\boldsymbol{\nabla}$ is the spatial gradient operator parallel to the boundary; and $\boldsymbol{v}$ is the interior velocity vector parallel to the boundary. The velocity anomaly may be represented by a line of sinks and sources that, at second order, generate gravity waves similar to that illustrated by Hurley & Imberger (1969) when an incident internal wave travels across small bottom undulations. Johns (1968) illustrated that using (1.1) as a bottom boundary condition induces a damping rate proportional to $\nu^{1/2}$. His method was extended to progressive internal waves in rotating fluids by Dore (1968), and Mei & Liu (1973) further showed that the velocity anomaly creates an energy flux into the boundary layer.

On the other hand the spin-down of a steady circulation or very low-frequency motions in a rotating basin is achieved by the Ekman pumping stretching (or squashing) the water column and inducing circular flow that cancels the existing circulation through the conservation of potential vorticity (e.g. Greenspan 1968; Benton & Clark 1974; Duck & Foster 2001). Spin-down induces fast damping ($\propto \nu^{1/2}$), compared to damping due to diffusion of momentum, the rate of which is proportional to ν (Benton & Clark 1974; Duck & Foster 2001). The Ekman pumping velocity can be calculated by the Ekman compatibility condition (Greenspan 1968):

$$w_E = \sqrt{\frac{\nu}{2f}}(\boldsymbol{\nabla} \times \boldsymbol{v}), \qquad (1.2)$$

where w_E is the Ekman pumping velocity and f is the Coriolis parameter or inertial frequency (twice the angular velocity of the basin). In a stratified fluid, the motion in the interior is not completely brought to rest by such a mechanism, as the stratification prevents the Ekman transport from moving up or down the vertical sidewall boundary layer; a diffusion mechanism is required to complete the damping (Benton & Clark 1974; Duck & Foster 2001).

Low-frequency motions such as shelf waves and Kelvin waves are spun-down by the same mechanism, although the unsteady inertia slightly modifies the process (Gill 1982). For a flat-bottomed basin, the compatibility condition extended to low-frequency motions is given by (Gill 1982)

$$\left(\frac{\partial^2}{\partial t^2} + f^2\right) w_E = \frac{\partial}{\partial t}(\nabla \cdot \boldsymbol{\tau}) + f(\nabla \times \boldsymbol{\tau}), \qquad (1.3)$$

where $\boldsymbol{\tau}$ is the bottom-shear-stress vector.

Interestingly, if we note that the bottom shear stress under the Stokes and Ekman boundary layers is $\sqrt{i\nu\omega}\boldsymbol{v}$ and $\sqrt{\nu f/2}\boldsymbol{v}$, respectively, (1.3) reduces to (1.1) and (1.2) in the high- and low-frequency limits. This suggests that damping of rotating basin-scale internal waves may possibly be modelled by coupling the velocity anomaly at the top of the boundary layers with the interior wave motion; the damping mechanism would then be the combination of the internal-wave cancelling and spin-down. Brink (1988) applied (1.3) to super-inertial gravity waves, although his solution was confined to progressive super-inertial gravity waves.

This study is aimed at obtaining an understanding of the fundamental processes that determine the observed damping rates of rotating basin-scale internal waves. In order to better illustrate the damping mechanisms, we limit our analysis to a flat-bottomed basin with vertical walls and constant rotation, containing a weakly stratified fluid (in the Boussinesq sense) with constant small viscosity. The solution is obtained through a perturbation analysis, assuming that the rotation rate is finite and the viscosity is small (e.g. van Dyke 1964). Strictly speaking, this approach has limited applicability to variable bottom basins because, when viscosity is zero, they support singular wave structures (wave attractors) in addition to regular standing wave modes (e.g. Maas & Lam 1995). However, the singular wave structures tend to become regular (singular modes) and to be damped faster than the standing wave modes as viscosity increases (Dintrans, Rieutord & Valdettaro 1999). In fact, both field data and three-dimensional numerical simulations have shown resonant responses of internal waves with distinct frequencies and structures in lakes (e.g. Hodges *et al.* 2000; Antenucci & Imberger 2003; Shimizu & Imberger 2008). Therefore, it is more relevant to use internal-wave solutions with distinct frequencies and continuous structures to obtain a fundamental understanding of damping mechanisms of internal waves in real lakes.

The paper is structured as follows. First, we derive the dynamics of the oscillatory boundary layers on the flat bottom and the vertical sidewall in a stratified rotating basin. Then, a perturbation method is developed that incorporates the velocity anomaly at the top of the boundary layers (hereafter referred to as the Ekman normal velocity) as a boundary condition into the basin-scale internal waves in the basin's interior. Next, the resulting perturbation method is applied to a non-rotating rectangular basin to illustrate the internal-wave-cancelling concept, and then this is generalized to the case in which both the internal-wave cancelling and spin-down contribute to the damping. The limitation and possible extension of the method proposed in this paper are discussed at the end.

2. Governing equations and scaling

Consider the damping of small-amplitude basin-scale internal waves in a shallow basin having vertical sidewalls and rotating parallel to the vertical axis with an angular frequency $f/2$ (f is assumed positive throughout this paper). Let z be the upward coordinate, with origin at the water surface, and x and y be horizontal coordinates

fixed to the rotating frame of reference. In order to separate the hydrostatic pressure field from the solution, we set the density and pressure such that

$$\rho^*(\boldsymbol{x}^*, t^*) = \rho_0^* + \rho_e^*(z^*) + \rho'^*(\boldsymbol{x}^*, t^*), \tag{2.1a}$$

$$p^*(\boldsymbol{x}^*, t^*) = p_e^*(z^*) + p'^*(\boldsymbol{x}^*, t^*), \tag{2.1b}$$

where $\boldsymbol{x} = (x, y, z)$ is the Cartesian coordinate vector; t is the time; ρ is the density; and p is the pressure. Variables with the subscripts 0 and e represent a nominal value and vertical variations at equilibrium, respectively. The prime on a variable denotes variation due to the motion, and * in the superscript indicates a dimensional variable. Substituting (2.1) into the Navier–Stokes equations, subtracting the hydrostatic pressure balance and assuming that the stratification is weak ($\rho'^*, \rho_e^* \ll \rho_0^*$) and that the fluid has a constant kinematic viscosity ν, and diffusivity of mass κ, the governing equations for the wave motion become

$$\nabla \cdot \boldsymbol{v}^* = 0, \tag{2.2a}$$

$$\frac{\partial \rho'^*}{\partial t^*} + \boldsymbol{v}^* \cdot \nabla \rho'^* = \frac{\rho_0^*}{g} N^{*2} w^* + \kappa \nabla^2 \rho'^*, \tag{2.2b}$$

$$\frac{\partial \boldsymbol{v}^*}{\partial t^*} + \boldsymbol{v}^* \cdot \nabla \boldsymbol{v}^* = -\frac{1}{\rho_0^*} \nabla p'^* - f(\hat{\boldsymbol{k}} \times \boldsymbol{v}^*) - \frac{g}{\rho_0^*} \rho'^* \hat{\boldsymbol{k}} + \nu \nabla^2 \boldsymbol{v}^*, \tag{2.2c}$$

where $\hat{\boldsymbol{k}}$ is the vertical unit vector; $\boldsymbol{v} = (u, v, w)$ is the velocity vector; g is the acceleration due to gravity;

$$N^*(z^*) = \sqrt{-\frac{g}{\rho_0^*} \frac{\partial \rho_e^*}{\partial z^*}} \tag{2.3}$$

is the buoyancy frequency; and ∇ is the spatial differential operator.

Further, we assume that the basin-scale internal waves have an angular frequency $O(\omega_0)$ and a small isopycnal displacement $O(a_0)$. The basin is assumed to have a flat bottom, vertical sidewalls and a depth H that is small compared to the horizontal length scale L but large compared to a_0. The basin is assumed filled with a continuously stratified fluid with a typical buoyancy frequency N_0. Given these scales, we may introduce the following non-dimensional variables:

$$(x, y, z) = \left(\frac{x^*}{L}, \frac{y^*}{L}, \frac{z^*}{H}\right), \tag{2.4a}$$

$$(u, v, w) = \left(\frac{u^*}{a_0\omega_0}, \frac{v^*}{a_0\omega_0}, \frac{w^*}{a_0\omega_0 A}\right), \tag{2.4b}$$

$$t = \omega_0 t^*, \tag{2.4c}$$

$$N = \frac{N^*}{N_0}, \tag{2.4d}$$

where the scale for the vertical velocity was determined by balancing the terms in (2.2a) and $A = H/L$ is the aspect ratio of the basin, assumed to be small. Substituting (2.4) into (2.2b, c) and balancing the unsteady terms with the first term on the right-hand side in (2.2b) and the pressure term in (2.2c) requires the density and pressure

to be non-dimensionalized as follows:

$$\rho' = \frac{g\rho'^*}{\rho_0^* N_0^2 a_0 A},$$ (2.5a)

$$p' = \frac{p'^*}{\rho_0^* a_0 \omega_0^2 L}.$$ (2.5b)

Given our assumption that $A \ll 1$ and $a_0 \ll H$, it follows that $a_0/L \ll 1$, and so the nonlinear terms in (2.2) that are $O(a_0/L)$ may be neglected. With this assumption, (2.2a, c) becomes

$$\frac{\partial u}{\partial x} + \frac{\partial v}{\partial y} + \frac{\partial w}{\partial z} = 0,$$ (2.6a)

$$\frac{\partial \rho'}{\partial t} = N^2 w + \frac{E}{Pr S}\left[A^2\left(\frac{\partial^2 \rho'}{\partial x^2} + \frac{\partial^2 \rho'}{\partial y^2}\right) + \frac{\partial^2 \rho'}{\partial z^2}\right],$$ (2.6b)

$$\frac{\partial u}{\partial t} = -\frac{\partial p'}{\partial x} + \frac{1}{S}v + \frac{E}{S}\left[A^2\left(\frac{\partial^2 u}{\partial x^2} + \frac{\partial^2 u}{\partial y^2}\right) + \frac{\partial^2 u}{\partial z^2}\right],$$ (2.6c)

$$\frac{\partial v}{\partial t} = -\frac{\partial p'}{\partial y} - \frac{1}{S}u + \frac{E}{S}\left[A^2\left(\frac{\partial^2 v}{\partial x^2} + \frac{\partial^2 v}{\partial y^2}\right) + \frac{\partial^2 v}{\partial z^2}\right],$$ (2.6d)

$$A^2\frac{\partial w}{\partial t} = -\frac{\partial p'}{\partial z} - \frac{B}{S^2}\rho' + \frac{EA^2}{S}\left[A^2\left(\frac{\partial^2 w}{\partial x^2} + \frac{\partial^2 w}{\partial y^2}\right) + \frac{\partial^2 w}{\partial z^2}\right],$$ (2.6e)

where $E = \nu\left(f H^2\right)^{-1}$ is the Ekman number; $S = f^{-1}\omega_0$ is the Burger number; $B = f^{-2} N_0^2 A^2$ is the stratification parameter; and $Pr = \nu/\kappa$ is the Prandtl number. The terms $O(A^2)$ are retained as they enter the force balance in the sidewall boundary layers, discussed later. Note that the parameter (E/S) is $\nu(\omega_0 H^2)^{-1}$ and independent of f.

Note that the angular frequency of basin-scale internal waves are $O(C/L)$, where C is the celerity of internal wave of interest (see §4.1 for calculation of C); so S may also be defined as $C(f L)^{-1}$ (see also Antenucci & Imberger 2001; Stoker & Imberger 2003). Note also that the second term on the right-hand side of (2.6e) has to be $O(1)$ for internal waves, implying $B = O(S^2)$. Assuming small viscosity and a shallow basin, we consider the parameter ranges $(E/S) \ll 1$, $A \ll 1$ and $B = O(S^2)$ in this paper. It is assumed that the axis of rotation is parallel to the vertical in the above equations, but the results are also applicable when the axis of rotation is tilted, provided that $(A/S) \ll 1$ and that the axis of rotation is not too close to the horizontal.

3. Ekman normal velocities induced by oscillatory boundary layers

By way of introduction, we shall consider the boundary layer formed on the flat bottom and the plane vertical sidewall forced by basin-scale internal waves. The solutions may be applied locally to curved sidewalls in a circular basin assuming the boundary layer is thin compared to the radius of curvature.

3.1. *Bottom boundary layer*

In order to focus on an oscillatory boundary layer on a flat bottom, we stretch the vertical coordinate and vertical velocity so that we get a balance between the vertical diffusion terms in (2.6c, d) and the unsteady terms; $Z = (E/S)^{-1/2}(z + 1)$, and (2.6a) implies $W = (E/S)^{-1/2}w$. Substituting the stretched variables into (2.6e) and neglecting all terms smaller than or equal to $O([E/S]^{1/2})$ shows that the pressure does not vary

across the bottom boundary layer, and the flow in the bottom boundary layer is, to first order, horizontal. In order to simplify the solution process, it is convenient to consider the deviation of boundary-layer velocity from the far-field value (i.e. the Ekman velocity; Gill 1982), such as $u_E = u - u_I$, where the subscripts E and I represent the Ekman and far-field values, respectively. We seek a periodic solution of the form

$$\varphi(\boldsymbol{x}, t) = \varphi(\boldsymbol{x})\,e^{i\omega t}, \tag{3.1}$$

where φ represents any of the variables and ω is the angular frequency of the parent wave in the interior (determined in §4.1) and is assumed to scale with ω_0. Here φ, on the right-hand side, is a complex variable, and the conjugate is omitted for simplicity. The conjugate solution appears naturally in the derivation below, as internal-wave modes occur as conjugate pairs (see (4.12)). Assuming such a solution exists and neglecting all terms smaller than or equal to $O([E/S]^{1/2})$, (2.6c, d) leads to the following expressions for the Ekman velocities:

$$i\omega u_E = \frac{1}{S}v_E + \frac{\partial^2 u_E}{\partial Z^2}, \quad i\omega v_E = -\frac{1}{S}u_E + \frac{\partial^2 v_E}{\partial Z^2}. \tag{3.2}$$

Note that pressure terms do not appear explicitly, as the pressure gradient balances with the unsteady inertia and the Coriolis forces based on the far-field velocities. The no-slip condition at the bottom requires

$$(u_E, v_E) = -(u_I, v_I) \text{ at } Z = 0, \tag{3.3}$$

and the Ekman velocity must vanish away from the bottom so the velocity in the boundary layer matches the far-field velocity,

$$(u_E, v_E) = (0, 0) \text{ at } Z \to \infty, \tag{3.4}$$

leading to the following solution (see Defant 1961 and the references therein):

$$u_E = -\frac{1}{2}[(e^{-\beta_- Z} + e^{-\beta_+ Z})u_I - i(e^{-\beta_- Z} - e^{-\beta_+ Z})v_I], \tag{3.5a}$$

$$v_E = -\frac{1}{2}[(e^{-\beta_- Z} + e^{-\beta_+ Z})v_I + i(e^{-\beta_- Z} - e^{-\beta_+ Z})u_I], \tag{3.5b}$$

where $\beta_\pm = \sqrt{i(\omega \pm S^{-1})}$. The solution represents two counter-rotating components with different vertical scales, $|\omega + S^{-1}|^{-1/2}$ and $|\omega - S^{-1}|^{-1/2}$, for the cyclonic (rotating in the same direction as the basin) and anticyclonic components, respectively (Defant 1961; Mofjeld 1980). When the frequency is much higher than the inertial (or $S \gg 1$), the solution reduces to the Stokes oscillatory boundary layer, whereas when the frequency is much lower than the inertial (or $S \ll 1$), it reduces to the Ekman layer (figure 1). The horizontal Ekman transport, q_{Ex} and q_{Ey} (scales with $[\nu\omega_0]^{1/2} a_0$), is obtained by vertically integrating (3.5a, b):

$$q_{Ex} = \frac{i\omega\gamma_{bl} + S^{-1}\gamma_{bt}}{\omega^2 - S^{-2}}u_I + \frac{S^{-1}\gamma_{bl} - i\omega\gamma_{bt}}{\omega^2 - S^{-2}}v_I, \tag{3.6a}$$

$$q_{Ey} = \frac{i\omega\gamma_{bl} + S^{-1}\gamma_{bt}}{\omega^2 - S^{-2}}v_I - \frac{S^{-1}\gamma_{bl} - i\omega\gamma_{bt}}{\omega^2 - S^{-2}}u_I, \tag{3.6b}$$

where

$$\gamma_{bl} = \frac{1}{2}(\beta_- + \beta_+), \quad \gamma_{bt} = \frac{i}{2}(\beta_- - \beta_+). \tag{3.7}$$
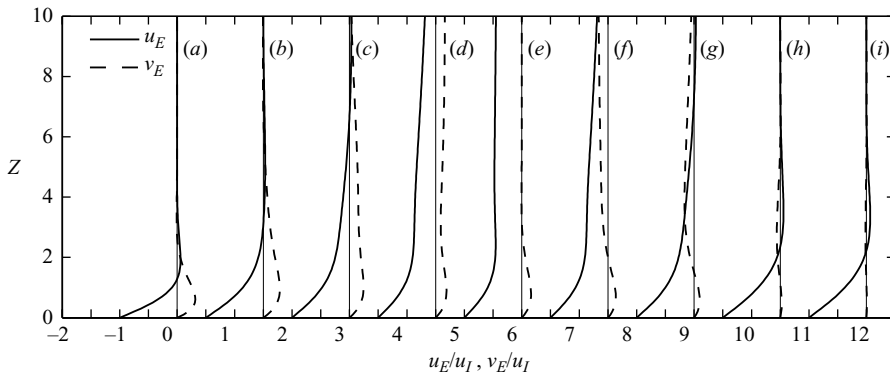
FIGURE 1. The Ekman velocities (u_E, v_E) when $(u_I, v_I) = (1, 0)$ and $t = 0$ (see (3.5)). Profiles (*a*)–(*i*) correspond to $S\omega = f^{-1}\omega^* = 0.30, 0.70, 0.90, 0.99, 1.00, 1.01, 1.10$ and 3.00 with 1.5 offset for each profile. Profiles (*a*) and (*i*) are almost identical to the Ekman layer and Stokes layer, respectively. Note the sharp transition of the structure near $S\omega = 1.00$.
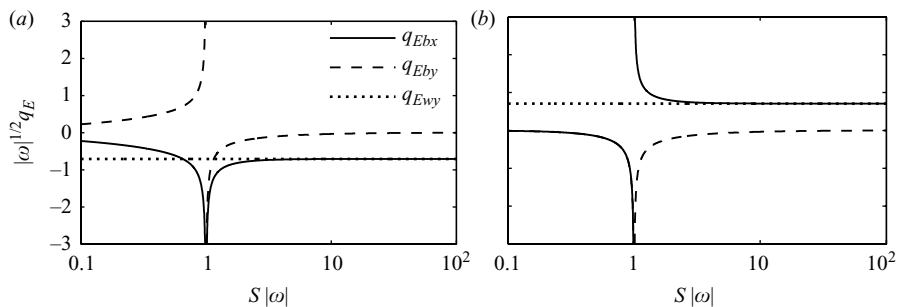

FIGURE 2. The Ekman transport in the rotating bottom boundary layer, (q_{Ebx}, q_{Eby}), and sidewall boundary layer, q_{Ewy}, when $(u_I, v_I) = (1, 0)$. (*a*) Real part (in phase with the far-field flow) and (*b*) imaginary part (quarter-period ahead of the far-field flow). In (*b*), the solid and dashed lines coincide for $S|\omega| < 1$.

The Ekman transport becomes large and exhibits a jump in phase when the frequency is equal to the inertial frequency (figure 2). The Ekman normal velocity may be obtained by vertically integrating the Ekman part of (2.6*a*) and substituting (3.6*a, b*) into the equation, yielding

$$w_E = -\left(\frac{E}{S}\right)^{1/2}\left[\frac{\mathrm{i}\omega\gamma_{bl} + S^{-1}\gamma_{bt}}{\omega^2 - S^{-2}}\left(\frac{\partial u_I}{\partial x} + \frac{\partial v_I}{\partial y}\right) + \frac{S^{-1}\gamma_{bl} - \mathrm{i}\omega\gamma_{bt}}{\omega^2 - S^{-2}}\left(\frac{\partial v_I}{\partial x} - \frac{\partial u_I}{\partial y}\right)\right] \tag{3.8}$$

3.2. *Sidewall boundary layer*

It is known that a sidewall boundary layer, forced by gravity waves, is the Stokes layer (e.g. Ursell 1952), but when the flow becomes steady, it becomes the sidewall boundary layers derived by Stewartson (1957) and Barcilon & Pedlosky (1967*a, b*) depending on relative strength of the stratification. Here we investigate the sidewall-boundary-layer structure induced by rotating basin-scale internal waves when the no-slip boundary condition is imposed at the vertical-wall face. The coordinate x is taken as positive into the fluid. In order to balance the unsteady terms in (2.6*d*) with the diffusion terms normal to the wall, we stretch x using the Stokes-layer thickness as

$X = (E/S)^{-1/2} A^{-1}x$, and conservation of volume (2.6a) implies $U = (E/S)^{-1/2} A^{-1}u$. As already discussed, the factor (E/S) is independent of f. Substituting these stretched variables and neglecting terms smaller than or equal to $O([E/S]^{1/2})$ and $O(A^2)$, (2.6a–e) becomes

$$\frac{\partial U}{\partial X} + \frac{\partial v}{\partial y} + \frac{\partial w}{\partial z} = 0, \tag{3.9a}$$

$$i\omega\rho' = N^2 w + \frac{1}{Pr}\frac{\partial^2 \rho'}{\partial X^2}, \tag{3.9b}$$

$$0 = -\frac{\partial p'}{\partial X} + \frac{E^{1/2}A}{S^{3/2}}v, \tag{3.9c}$$

$$i\omega v = -\frac{\partial p'}{\partial y} - \frac{E^{1/2}A}{S^{3/2}}U + \frac{\partial^2 v}{\partial X^2}, \tag{3.9d}$$

$$0 = -\frac{\partial p'}{\partial z} - \frac{B}{S^2}\rho'. \tag{3.9e}$$

Equation (3.9c) indicates that the Coriolis force modifies the pressure across the boundary layer, whenever $E^{1/2}AS^{-3/2} = (\omega_0^{3/2}L)^{-1}\nu^{1/2}f \approx 1$. In what follows, we make the assumption that

$$EA^2 \ll S^3, \tag{3.10}$$

so that the pressure deviation from the equilibrium is constant across the layer. In order to solve (3.9a–e), we once again split the flow into the far-field flow and its deviation (i.e. $v_E = v - v_I$, $w_E = w - w_I$, $\rho'_E = \rho' - \rho'_I$). As the pressure deviation is constant across the layer and the interior pressure gradients in y and z balance with the unsteady inertia and gravity in the far field, (3.9e) implies $\rho'_E = 0$, and together this yields $w_E = 0$ from (3.9b). From this it follows that we only need to consider horizontal motion along the vertical wall, governed by (3.9d). The solution to the Ekman part of (3.9d) with the boundary conditions

$$v_E = -v_I \quad \text{at } X = 0, \tag{3.11a}$$
$$v_E = 0 \quad \text{as } X \to \infty \tag{3.11b}$$

is given by the Stokes-oscillatory-boundary-layer solution (e.g. Pedlosky 1979). The Ekman transport and Ekman normal velocity may be calculated by integrating the solution across the boundary layer. Using (3.9a), this yields

$$q_{Ey} = \frac{i\gamma_{sw}}{\omega}v_I, \quad q_{Ez} = 0, \tag{3.12}$$

$$u_E = -\left(\frac{E}{S}\right)^{1/2} A\frac{i\gamma_{sw}}{\omega}\frac{\partial v_I}{\partial y}, \tag{3.13}$$

where q_{Ez} is the vertical Ekman transport and

$$\gamma_{sw} = \sqrt{i\omega}. \tag{3.14}$$

Although the vertical sidewall boundary layer does not support the vertical Ekman transport when the fluid is stratified, horizontal divergence of the Ekman transport does induce an Ekman normal velocity. Unlike in the bottom boundary layer, the Ekman transport in the vertical sidewall boundary layer does not show any transition at the inertial frequency (figure 2). It is important to note that although stratification

does not appear in the boundary-layer solution explicitly, it suppresses the vertical motion in the sidewall boundary layer.

3.3. *Bottom-corner region*

An important implication of the above results is that the horizontal bottom Ekman transport (q_{Ex} in (3.6a) with $u_I = 0$ and $v_I \neq 0$) cannot simply enter the vertical sidewall boundary layer, as, from (3.12b), $q_{Ez} = 0$ there. As in the stratified spin-down problems, the horizontal bottom Ekman transport must somehow be communicated into the interior to satisfy the conservation of mass (e.g. Walin 1969; Benton & Clark 1974). The bottom-corner region effectively acts as the sinks and/or sources of fluid for the interior flow (see e.g. figures 2 and 5 in Walin 1969). In our case, the sinks and sources are oscillating in time, which may induce source flow when the frequency is low as in stratified spin-down (Walin 1969) but may emit internal-wave rays when the frequency is higher than the inertial frequency (Lighthill 1978; Gill 1982). It is not easy to obtain analytical solutions for the flow details in the corner region (Walin 1969); however, considering the limiting case of small viscosity ($E/S \to 0$), the width of the corner region become infinitely small (except when ω is very close to but above S^{-1}), as shown in appendix D. This indicates that the sinks and sources may be conveniently modelled using the Dirac delta function δ representation as suggested by Spence, Foster & Davis (1992) and Duck & Foster (2001). As the sidewall boundary layer does not support the Ekman transport (see (3.12)) and the fluid is incompressible, the additional vertical Ekman normal velocity at the bottom corner must be equal to the horizontal Ekman transport at the corner, determined from (3.6a) by setting $u_I = 0$:

$$w_E = \left(\frac{E}{S} \right)^{1/2} \frac{S^{-1}\gamma_{bl} - \mathrm{i}\omega\gamma_{bt}}{\omega^2 - S^{-2}} v_I \delta(x). \tag{3.15}$$

We use this representation to obtain analytical solutions and to illustrate the roles of the corner sinks and sources. This treatment is rather qualitative, and the length scale of the sinks and sources may need to be accounted for, particularly when internal-wave rays are emitted from the corner region. (Otherwise the interior solutions may become singular). Qualitatively, this may be achieved by terminating a series expansion at the wavenumber corresponding to the length scale of the sinks and sources (Walin 1969). Note that the Ekman velocity affects the interior flow only as a volume source, not as a momentum source.

4. Perturbation analysis of damped internal waves

We employ a perturbation analysis to obtain a solution for damped internal waves as suggested by Greenspan (1968), Johns (1968) and Duck & Foster (2001); viscosity is assumed small so that it affects the solution only through the Ekman normal velocities. The solution method exploits the orthogonality of the three-dimensional normal modes that make up the inviscid solution of (2.6); the orthogonality is derived in appendix A. Similar methods have been used to calculate damped coastal trapped waves by Brink & Allen (1978), Brink (1982) and Clarke & Van Gorder (1986). The derivation below, given in Cartesian coordinates, is valid for basins of any arbitrary horizontal shape provided that the following conditions are met: the bottom is flat; the sidewall is vertical; and the assumptions we have made so far are satisfied.

Consider a basin-scale internal wave with the angular frequency ω as a solution to (2.6). Neglecting the diffusion terms and the terms $O(A^2)$, (2.6b) and (2.6e) may be

combined to yield

$$0 = -i\omega \frac{\partial p'}{\partial z} - \frac{BN^2}{S^2} w. \tag{4.1}$$

Deleting w from the above equation and (2.6a) yields

$$-i\omega \frac{\partial}{\partial z} \left(\frac{S^2}{BN^2} \frac{\partial p'}{\partial z} \right) = - \left(\frac{\partial u}{\partial x} + \frac{\partial v}{\partial y} \right). \tag{4.2}$$

Assuming small displacement at the surface, the surface boundary condition may be assumed to be given by

$$p' = \frac{c_0^2 w}{i\omega} = -\frac{c_0^2 S^2}{BN^2} \frac{\partial p'}{\partial z} \quad \text{at } z = 0, \tag{4.3}$$

where c_0 is the celerity for surface waves and (4.1) is used to relate w with p'. The boundary conditions at the bottom and sidewall are determined by the Ekman normal velocities as

$$-i\omega \frac{S^2}{BN^2} \frac{\partial p'}{\partial z} = w_E \quad \text{at } z = -1, \tag{4.4a}$$

$$u\hat{n}_x + v\hat{n}_y = -u_{En} \quad \text{at the sidewall}, \tag{4.4b}$$

where $(\hat{n}_x, \hat{n}_y)$ is the horizontal unit outward normal vector at the vertical sidewall; w_E is obtained from (3.8) and (3.15); and u_{En} is the Ekman normal velocity, normal to the sidewall, equal to u_E in (3.13). In order to take advantage of the orthogonality of the inviscid modes later, we add (4.2) and (4.4a) multiplied by $\delta(z+1)$. Then, following Platzman (1972) and Shimizu, Imberger & Kumagai (2007), we write the resulting equation with (2.6c, d) as a matrix equation:

$$\omega M\xi = K\xi + f_b, \tag{4.5a}$$

$$\xi = \begin{pmatrix} p' \\ u \\ v \end{pmatrix}, \tag{4.5b}$$

$$f_b = -i \begin{pmatrix} \delta(z+1) w_E \\ 0 \\ 0 \end{pmatrix}, \tag{4.5c}$$

$$M = \begin{pmatrix} -\left[\frac{\partial}{\partial z} + \delta(z+1) \right] \left(\frac{S^2}{BN^2} \frac{\partial}{\partial z} \right) & 0 & 0 \\ 0 & 1 & 0 \\ 0 & 0 & 1 \end{pmatrix}, \tag{4.5d}$$

$$K = i \begin{pmatrix} 0 & \frac{\partial}{\partial x} & \frac{\partial}{\partial y} \\ \frac{\partial}{\partial x} & 0 & -\frac{1}{S} \\ \frac{\partial}{\partial y} & \frac{1}{S} & 0 \end{pmatrix}. \tag{4.5e}$$

We solve the above equation for (p', u, v) with the boundary conditions (4.3) and (4.4) by expanding the variables in a perturbation series in the small parameter (E/S).

4.1. *Inviscid interior solutions*

Using vertical modes, the homogeneous solutions to (4.5) may be written as (e.g. Gill 1982)

$$\tilde{\xi}_{(l,m)}^{(0)} = \begin{pmatrix} \tilde{p}'^{(0)}_{(l,m)}(x,y,z) \\ \tilde{u}^{(0)}_{(l,m)}(x,y,z) \\ \tilde{v}^{(0)}_{(l,m)}(x,y,z) \end{pmatrix} = \phi_l(z) \begin{pmatrix} c_l^2 \eta_{(l,m)}(x,y) \\ u_{(l,m)}(x,y) \\ v_{(l,m)}(x,y) \end{pmatrix}, \tag{4.6}$$

where the superscript 0 is used to denote inviscid modes; l and m in the subscript denote lth vertical and mth horizontal modes; ϕ_l denotes the vertical modes in a continuously stratified fluid; $\eta_{(l,m)}$ represents horizontal variation of the pressure and $u_{(l,m)}$ and $v_{(l,m)}$ represent horizontal variations of velocities; and c_l is the celerity of lth vertical mode (non-dimensionalized by $L\omega_0$). The surface mode is given by $l = 0$, and $l > 0$ represent internal-wave modes.

The vertical modes ϕ_l and their associated celerities c_l are determined from the solution of (e.g. Gill 1982)

$$c_l^2 \frac{\partial}{\partial z}\left(\frac{S^2}{BN^2} \frac{\partial \phi_l}{\partial z} \right) + \phi_l = 0 \tag{4.7}$$

with the boundary conditions

$$\frac{c_0^2 S^2}{BN^2} \frac{\partial \phi_l}{\partial z} + \phi_l = 0 \quad \text{at} \quad z = 0, \tag{4.8a}$$

$$\frac{\partial \phi_l}{\partial z} = 0 \quad \text{at} \quad z = -1. \tag{4.8b}$$

The vertical modes satisfy the orthogonality condition (e.g. Gill 1982)

$$\int_{-1}^{0} \phi_p \phi_l \, \mathrm{d}z = \rho_{KE(l)} \delta_{p,l}, \tag{4.9}$$

where $\delta_{i,j}$ ($=1$ if $i = j$ but 0 otherwise) is the Kronecker delta and $\rho_{KE(l)}$ (scales with $\rho_0^* H$) is the arbitrary normalization factor for lth vertical mode.

The horizontal modal structures or eigenfunctions, $(\eta_{(l,m)}, u_{(l,m)}, v_{(l,m)})$, are determined from the shallow-water equations corresponding to individual vertical modes (e.g. Gill 1982),

$$i\omega_{(l,m)}^{(0)} \eta_{(l,m)} = -\left(\frac{\partial u_{(l,m)}}{\partial x} + \frac{\partial v_{(l,m)}}{\partial y} \right), \tag{4.10a}$$

$$i\omega_{(l,m)}^{(0)} u_{(l,m)} = -c_l^2 \frac{\partial \eta_{(l,m)}}{\partial x} + \frac{1}{S} v_{(l,m)}, \tag{4.10b}$$

$$i\omega_{(l,m)}^{(0)} v_{(l,m)} = -c_l^2 \frac{\partial \eta_{(l,m)}}{\partial y} - \frac{1}{S} u_{(l,m)}, \tag{4.10c}$$

with the boundary condition

$$u_{(l,m)}\hat{n}_x + v_{(l,m)}\hat{n}_y = 0 \text{ at the sidewall.} \tag{4.11}$$

The solutions represent the horizontal modes that have a distinct horizontal modal structure, $(\eta_{(l,m)}, u_{(l,m)}, v_{(l,m)})$, and an angular frequency $\omega_{(l,m)}^{(0)}$ (Proudman 1929; Platzman 1972; Shimizu *et al.* 2007). The solutions occur in conjugate pairs unless $\omega_{(l,m)}^{(0)} = 0$. We designate a solution with positive angular frequency with

a plus sign in the subscript, $(\omega^{(0)}_{(l,+m)}, \eta_{(l,+m)}, u_{(l,+m)}, v_{(l,+m)})$, and its conjugate pair, $(\omega^{(0)}_{(l,-m)}, \eta_{(l,-m)}, u_{(l,-m)}, v_{(l,-m)})$, with a minus sign. The relationship between the two is given by (Platzman 1972)

$$\left(\omega^{(0)}_{(l,+m)}, \eta_{(l,+m)}, u_{(l,+m)}, v_{(l,+m)}\right) = \left(-\omega^{(0)}_{(l,-m)}, \bar{\eta}_{(l,-m)}, \bar{u}_{(l,-m)}, \bar{v}_{(l,-m)}\right), \tag{4.12}$$

where the overbar stands for the complex conjugate; if the subscript does not have a plus or minus sign, then the relationship applies to both the modes. Distinction between $+m$ and $-m$ modes is necessary when the horizontal modes are used for a series expansion (Platzman 1984; see (4.17)). Equation (4.10b, c) suggests that c_l should be $O(1)$ for the wave of interest, as we are interested in internal gravity waves influenced by rotation. Therefore, we hereafter set $\omega_0 = L^{-1}C$, where C is the celerity of the wave of interest.

The three-dimensional modes satisfy the general orthogonality relationships of the form (see (A 11))

$$\int \left(\tilde{\boldsymbol{\xi}}^{(0)}_{(p,q)}{}^H \boldsymbol{M} \tilde{\boldsymbol{\xi}}^{(0)}_{(l,m)}\right) \mathrm{d}V = \tilde{e}_{(l,m)}\delta_{p,l}\delta_{q,m}, \tag{4.13a}$$

$$\int \left(\tilde{\boldsymbol{\xi}}^{(0)}_{(p,q)}{}^H \boldsymbol{K} \tilde{\boldsymbol{\xi}}^{(0)}_{(l,m)}\right) \mathrm{d}V = \omega^{(0)}_{(l,m)}\tilde{e}_{(l,m)}\delta_{p,l}\delta_{q,m}, \tag{4.13b}$$

where $\boldsymbol{\xi}$, $\boldsymbol{M}$ and $\boldsymbol{K}$ are defined in (4.5); H in the superscript stands for conjugate transpose; $\mathrm{d}V = \mathrm{d}x\,\mathrm{d}y\,\mathrm{d}z$ is the volume element; p and q in the subscript are modal indices that are independent of l and m; and $\tilde{e}_{(l,m)}$ (scaling with $\rho_0^* H C^2 a_0^2$) is an arbitrary normalization factor for the (l, m) mode. This is the norm that is equivalent to twice the total energy of the mode (see (A 5) and (A 11)).

4.2. *Correction to the inviscid basin-scale internal waves due to boundary-layer presence*

Since the Ekman normal velocities are $O([E/S]^{1/2})$, we focus on one mode, say the (l, m) mode, and look for small viscous corrections to the angular frequency and modal structure. The variables in (4.3)–(4.5) may be expanded as a perturbation series:

$$\omega = \omega^{(0)}_{(l,m)} + (E/S)^{1/2}\,\omega^{(1)}_{(l,m)} + \cdots, \tag{4.14a}$$

$$\boldsymbol{\xi} = \tilde{\boldsymbol{\xi}}^{(0)}_{(l,m)} + (E/S)^{1/2}\,\tilde{\boldsymbol{\xi}}^{(1)}_{(l,m)} + \cdots, \tag{4.14b}$$

$$u_{En} = \tilde{u}^{(0)}_{En(l,m)} + (E/S)^{1/2}\,\tilde{u}^{(1)}_{En(l,m)} + \cdots, \tag{4.14c}$$

$$w_E = \tilde{w}^{(0)}_{E(l,m)} + (E/S)^{1/2}\,\tilde{w}^{(1)}_{E(l,m)} + \cdots, \tag{4.14d}$$

where the superscript 1 indicates first-order viscous correction and $\tilde{u}^{(0)}_{En(l,m)}$ and $\tilde{w}^{(0)}_{E(l,m)}$ are determined from (3.8), (3.13) and (3.15) by setting $(u_I, v_I) = (\tilde{u}^{(0)}_{(l,m)}, \tilde{v}^{(0)}_{(l,m)})$. The first-order correction to the modal frequency $\omega^{(1)}_{(l,m)}$ is a complex variable, the real and imaginary parts of which give the first-order correction to the angular frequency and the damping rate, respectively. Substituting the above expansions into (4.5) and collecting the terms $O([E/S]^{1/2})$, we get

$$\omega^{(1)}_{(l,m)}\boldsymbol{M}\tilde{\boldsymbol{\xi}}^{(0)}_{(l,m)} + \omega^{(0)}_{(l,m)}\boldsymbol{M}\tilde{\boldsymbol{\xi}}^{(1)}_{(l,m)} = \boldsymbol{K}\tilde{\boldsymbol{\xi}}^{(1)}_{(l,m)} + \tilde{\boldsymbol{f}}^{(0)}_{b(l,m)}, \tag{4.15}$$

where $\tilde{\boldsymbol{f}}^{(0)}_{b(l,m)}$ is determined by substituting $\tilde{w}^{(0)}_{E(l,m)}$ into the definition given by (4.5c). The boundary conditions, (4.3) and (4.4), become

$$\tilde{p}'^{(1)}_{(l,m)} = -\frac{c_0^2 S^2}{BN^2}\frac{\partial \tilde{p}'^{(1)}_{(l,m)}}{\partial z} \quad \text{at } z = 0, \tag{4.16a}$$

$$-\mathrm{i}\omega\frac{S^2}{BN^2}\frac{\partial \tilde{p}'^{(1)}_{(l,m)}}{\partial z} = \tilde{w}^{(0)}_{E(l,m)} \qquad \text{at } z = -1, \tag{4.16b}$$

$$\tilde{u}^{(1)}_{(l,m)}\hat{n}_x + \tilde{v}^{(1)}_{(l,m)}\hat{n}_y = -\tilde{u}^{(0)}_{En(l,m)} \qquad \text{at the sidewall.} \tag{4.16c}$$

Since the inviscid solutions form a complete set of functions (see appendix A), the first-order correction to the modal structure, $\tilde{\boldsymbol{\xi}}^{(1)}_{(l,m)}$, can be expressed as a superposition of the inviscid modes:

$$\tilde{\boldsymbol{\xi}}^{(1)}_{(l,m)} = \sum_{s=0}^{\infty}\sum_{t=-\infty}^{+\infty} \tilde{\boldsymbol{\xi}}^{(0)}_{(s,t)}\tilde{b}_{(l,m)(s,t)}, \tag{4.17}$$

where $\tilde{b}_{(l,m)(s,t)}$ is the 'amplitude' of the (s,t) mode contained in the first-order correction to the (l,m) mode. Following Platzman (1984), the equations that determine $\omega^{(1)}_{(l,m)}$ and $\tilde{b}_{(l,m)(s,t)}$ can be obtained as follows. First, we multiply (4.15) by the complex conjugate of the modal-structure function of a particular inviscid mode, say the (p,q) mode, and integrate the resulting equation over the basin, yielding

$$\omega^{(1)}_{(l,m)} \int \left(\tilde{\boldsymbol{\xi}}^{(0)}_{(p,q)}{}^H \boldsymbol{M}\tilde{\boldsymbol{\xi}}^{(0)}_{(l,m)}\right)\mathrm{d}V + \omega^{(0)}_{(l,m)} \int \left(\tilde{\boldsymbol{\xi}}^{(0)}_{(p,q)}{}^H \boldsymbol{M}\tilde{\boldsymbol{\xi}}^{(1)}_{(l,m)}\right)\mathrm{d}V$$

$$= \int \left(\tilde{\boldsymbol{\xi}}^{(0)}_{(p,q)}{}^H \boldsymbol{K}\tilde{\boldsymbol{\xi}}^{(1)}_{(l,m)}\right)\mathrm{d}V + \int \left(\tilde{\boldsymbol{\xi}}^{(0)}_{(p,q)}{}^H \tilde{\boldsymbol{f}}^{(0)}_{b(l,m)}\right)\mathrm{d}V. \tag{4.18}$$

Second, we integrate the first term on the right-hand side by parts, so that (see (A 8))

$$\int \left(\tilde{\boldsymbol{\xi}}^{(0)}_{(p,q)}{}^H \boldsymbol{K}\tilde{\boldsymbol{\xi}}^{(1)}_{(l,m)}\right)\mathrm{d}V = -\mathrm{i}\oint\int_{-1}^{0} \left(\bar{\tilde{p}}'^{(0)}_{(p,q)}\tilde{u}^{(0)}_{En(l,m)}\right)\mathrm{d}z\,\mathrm{d}s + \int \left[\left(\boldsymbol{K}\tilde{\boldsymbol{\xi}}^{(0)}_{(p,q)}\right)^H\tilde{\boldsymbol{\xi}}^{(1)}_{(l,m)}\right]\mathrm{d}V, \tag{4.19}$$

where (4.16c) has been applied; ds is the length element along the sidewall; and the integral in the first term on the right-hand side is taken along the sidewall. Further, we expand $\tilde{\boldsymbol{\xi}}^{(1)}_{(l,m)}$ using (4.17) and then apply (4.13a) and the conjugate transpose of (4.13b) to the left-hand side of (4.18) and the second term on the right-hand side of (4.19), respectively, to get the equation

$$\omega^{(1)}_{(l,m)}\,\tilde{e}_{(l,m)}\delta_{p,l}\delta_{q,m} + \left(\omega^{(0)}_{(l,m)} - \omega^{(0)}_{(p,q)}\right)\tilde{e}_{(p,q)}\tilde{b}_{(l,m)(p,q)}$$

$$= -\mathrm{i}\oint\int_{-1}^{0} \left(\bar{\tilde{p}}'^{(0)}_{(p,q)}\tilde{u}^{(0)}_{En(l,m)}\right)\mathrm{d}z\,\mathrm{d}s + \int \left(\tilde{\boldsymbol{\xi}}^{(0)}_{(p,q)}{}^H \tilde{\boldsymbol{f}}^{(0)}_{b(l,m)}\right)\mathrm{d}V. \tag{4.20}$$

This equation may be decomposed into vertical modal components by substituting (4.6) and using the orthogonality of the vertical modes, (4.9), yielding

$$\omega^{(1)}_{(l,m)}\,\tilde{e}_{(p,q)}\delta_{p,l}\delta_{q,m} + \left(\omega^{(0)}_{(l,m)} - \omega^{(0)}_{(p,q)}\right)\tilde{e}_{(p,q)}\tilde{b}_{(l,m)(p,q)}$$

$$= -\mathrm{i}c_p^2\rho_{KE(l)}\oint \left(\bar{\eta}_{(p,q)}u^{sw}_{En(l,m)}\right)\mathrm{d}s\,\delta_{p,l}$$

$$-\mathrm{i}c_p^2\phi_p(-1)\phi_l(-1)\iint \left[\bar{\eta}_{(p,q)}\left(w^{wc}_{E(l,m)} + w^{sp}_{E(l,m)}\right)\right]\mathrm{d}x\,\mathrm{d}y. \tag{4.21}$$

In the above equation, $w_{E(l,m)}^{\text{iwc}}$, $w_{E(l,m)}^{sp}$ and $u_{En(l,m)}^{sw}$ are the bottom and sidewall Ekman normal velocities calculated from the compatibility conditions (3.8), (3.13) and (3.15):

$$w_{E(l,m)}^{\text{iwc}} = -\frac{\mathrm{i}\omega_{(l,m)}^{(0)}\gamma_{bl} + S^{-1}\gamma_{bt}}{\omega_{(l,m)}^{(0)}{}^2 - S^{-2}}\left(\frac{\partial u_{(l,m)}}{\partial x} + \frac{\partial v_{(l,m)}}{\partial y}\right), \tag{4.22a}$$

$$w_{E(l,m)}^{sp} = -\frac{S^{-1}\gamma_{bl} - \mathrm{i}\omega_{(l,m)}^{(0)}\gamma_{bt}}{\omega_{(l,m)}^{(0)}{}^2 - S^{-2}}$$
$$\times \left[\left(\frac{\partial v_{(l,m)}}{\partial x} - \frac{\partial u_{(l,m)}}{\partial y}\right) - \left(u_{(l,m)}\hat{s}_x + v_{(l,m)}\hat{s}_y\right)\delta\left(\boldsymbol{x} - \boldsymbol{x}_{sw}\right)\right], \tag{4.22b}$$

$$u_{En(l,m)}^{sw} = -A\frac{\mathrm{i}\gamma_{sw}}{\omega_{(l,m)}^{(0)}}\left(\frac{\partial u_{(l,m)}}{\partial x}\hat{s}_x + \frac{\partial v_{(l,m)}}{\partial y}\hat{s}_y\right) \text{ at the sidewall,} \tag{4.22c}$$

where $(\hat{s}_x, \hat{s}_y)$ is the horizontal unit vector tangential to the sidewall (positive when the wall is to the right) and $\boldsymbol{x}_{sw}$ indicates the location of the sidewall. We have rather arbitrarily split the bottom Ekman normal velocity into two parts, such that $w_{E(l,m)}^{sp}$ accompanies the sinks and sources at the bottom corner and $w_{E(l,m)}^{\text{iwc}}$ is independent of it. As shown later, $w_{E(l,m)}^{\text{iwc}}$ and $w_{E(l,m)}^{sp}$ are related to the internal-wave cancelling and modified spin-down, respectively. Note that the integrals of $w_{E(l,m)}^{\text{iwc}}$ and $w_{E(l,m)}^{sp}$ over the basin vanish from the Gauss's and Stokes's theorems and the boundary condition (4.11), meaning that the mass in the interior (hence in the boundary layer) is conserved and that the sinks and sources at the corner are necessary to achieve this balance.

Setting $p = l$ and $q = m$ in (4.21) yields an expression for $\omega_{(l,m)}^{(1)}$. Noting that $\tilde{e}_{(l,m)}$ is twice the total energy and that the left-hand side is the complex rate of work done by the leading mode to the boundary layers (i.e. pressure times velocity normal to the boundary), it is seen that (4.21) is similar to the energy damping-rate calculation method (Lamb 1932) and the method suggested by Mei & Liu (1973), except that (4.21) is applicable to rotating basins. This method is efficient in calculating $\omega_{(l,m)}^{(1)}$, as it does not require knowledge about $\tilde{\boldsymbol{\xi}}_{(l,m)}^{(1)}$.

Taking $p \neq l$ or $q \neq m$ yields $\tilde{b}_{(l,m)(p,q)}$, and substituting the results back into (4.17) and then into (4.14b) gives the modal-structure correction. Note that we have $\tilde{b}_{(l,m)(l,m)} = 0$ by keeping the norm (the same form as the integral in left-hand side of (4.13a))

$$\int\left(\tilde{\boldsymbol{\xi}}_{(l,m)}{}^H \boldsymbol{M}\tilde{\boldsymbol{\xi}}_{(l,m)}\right)\mathrm{d}V, \tag{4.23}$$

the same with and without the first-order corrections (e.g. Kalaba, Spingarn & Tesfatsion 1981). Also note that there is always a possibility that $\tilde{b}_{(l,m)(p,q)}$ becomes very large when $\omega_{(l,m)}^{(0)} \approx \omega_{(p,q)}^{(0)}$ (see (4.21)), as the higher horizontal, higher vertical modes may have frequencies close to the leading wave in a continuously stratified basin. This, however, may not occur in reality, as higher modes are more susceptible to viscous damping in the interior, which is beyond the scope of the current analysis. The convergence of the modal expansion (4.17) is slow, as this method expresses velocities normal to the boundary by superposition of inviscid modes that themselves have zero velocity normal to the boundary; the boundary condition is satisfied only in an asymptotic sense, similar to the Fourier series reproducing discontinuities.

5. Internal-wave cancelling in a flat-bottomed rectangular basin

First we illustrate, by way of example, damping by the internal-wave cancelling of a vertical mode 1 basin-scale internal wave in a non-rotating rectangular basin of length L and width W, filled with a linearly stratified fluid (i.e. $N = 1$). Horizontal coordinates x and y are taken in the longitudinal and transverse directions, respectively, and the basin length is used as the horizontal length scale. Vertical modes were obtained by solving (4.7) and (4.8). For a vertical mode 1 internal wave, $C \approx N_0 H/\pi$, which yields $B \approx \pi^2 S^2$. To illustrate the process, the sidewall boundary layers are neglected, and only longitudinal oscillations are considered.

The horizontal modes for the longitudinal oscillations and the associated angular frequencies are

$$\eta_{(l,m)} = c_l^{-1} \cos(m\pi x), \tag{5.1a}$$

$$u_{(l,m)} = -i \sin(m\pi x), \tag{5.1b}$$

$$\omega_{(l,m)}^{(0)} = c_l m\pi, \tag{5.1c}$$

where m is an integer other than 0. (Note that the modes with $+m$ and $-m$ form a conjugate pair that satisfies (4.12).) The normalizing factors (4.13a) are

$$\tilde{e}_{(l,m)} = \rho_{KE(l)} A_h, \tag{5.2}$$

where $A_h = W/L$ is the horizontal aspect ratio of the basin. From (4.22a), the velocity, given by (5.1b), induces an Ekman normal velocity

$$w_{E(l,m)}^{iwc} = -\sqrt{i\omega_{(l,m)}^{(0)}} \eta_{(l,m)} \tag{5.3}$$

at the top of the bottom boundary layer, where $\gamma_{bl} = \sqrt{i\omega_{(l,m)}^{(0)}}$ and $\gamma_{bt} = 0$ are used, as the bottom boundary layer is a Stokes layer. Using (5.1)–(5.3), (4.21) becomes

$$\omega_{(l,m)}^{(1)} \delta_{p,l} \delta_{q,m} + \left(\omega_{(l,m)}^{(0)} - \omega_{(p,q)}^{(0)} \right) \tilde{b}_{(l,m)(p,q)} = i\sqrt{i\omega_{(l,m)}^{(0)}} \frac{f_{(p,l)}^V}{2} \delta_{q,\pm m}, \tag{5.4}$$

where $\delta_{q,\pm m} = 1$ only if $q = +m$ or $-m$ and

$$f_{(p,l)}^V = \frac{\phi_p(-1)\phi_l(-1)}{\rho_{KE(p)}} \frac{c_p}{c_l}. \tag{5.5}$$

Note that unlike a rectangular basin with a rigid lid, the natural frequencies and modal structures were distinct due to the presence of the free surface (see (4.8a)), making $\omega_{(l,m)}^{(0)} - \omega_{(p,q)}^{(0)}$ non-zero except when $(p,q) = (l,m)$.

Setting $(p,q) = (l,m)$ in (5.4) gives $\omega_{(l,m)}^{(1)}$ that has a negative real part and positive imaginary part of equal magnitudes, indicating the bottom boundary layer induces retardation of the oscillation and damping. The damping is proportional to $\sqrt{\omega_{(l,m)}^{(0)}}$, so that waves with higher frequencies are damped faster, but damping per period is smaller for such waves. For linear stratification, there is no preferential damping of particular vertical internal-wave modes, as (5.5) gives $f_{(l,l)}^V = 2$ for all the vertical modes. The homogeneous case may be recovered by setting $C = (gH)^{1/2}$, $\phi_0(-1) = 1$, $\rho_{KE(0)} = 1$ and $f_{(0,0)}^V = 1$; this damping rate agrees with the results by Hunt (1952) and van Dorn (1966) in the shallow-water limit, after converting their spatial damping rates to temporal damping rates.

The dissipative structure of the fundamental-mode internal wave may be calculated by taking $p \neq l$ or $q \neq m$ to obtain $\tilde{b}_{(l,m)(p,q)}$ and substituting the results into (4.17).
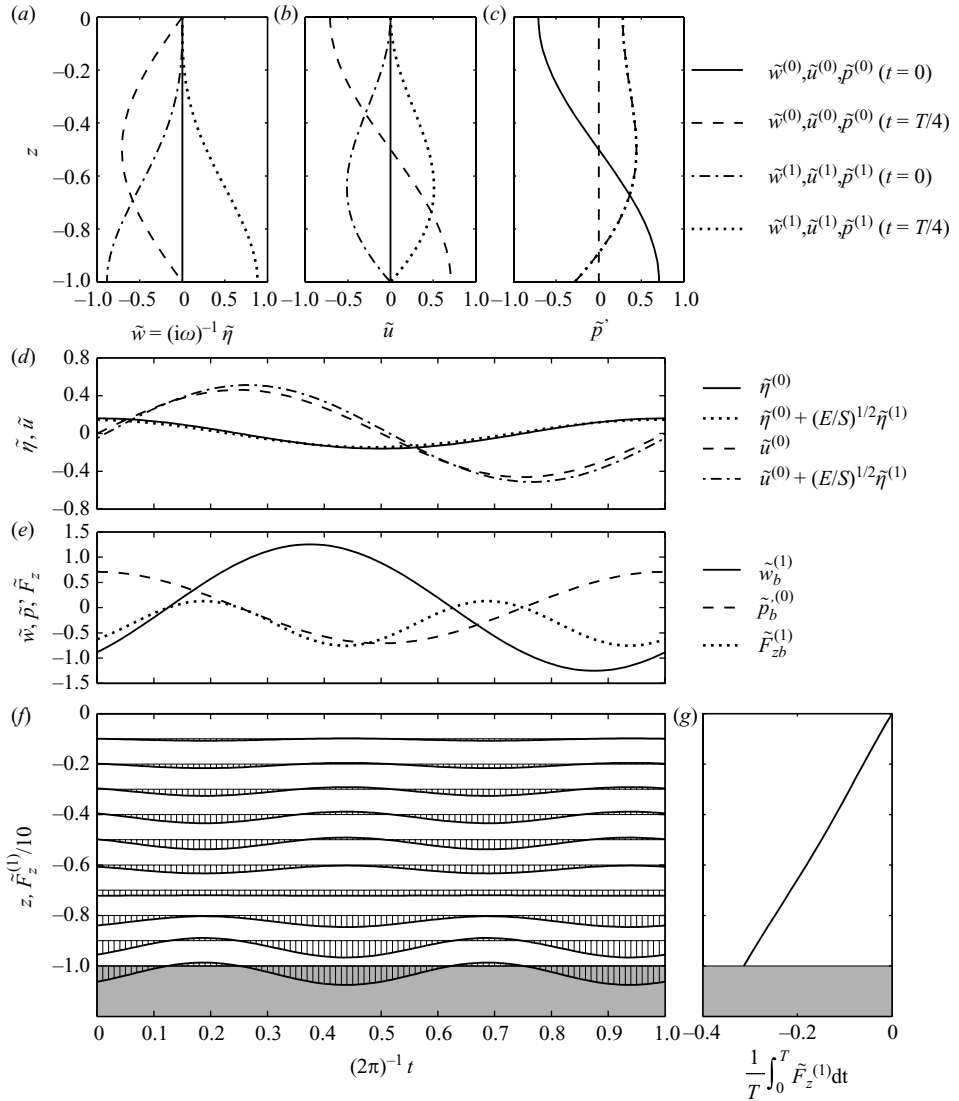
FIGURE 3. The internal-wave cancelling of the fundamental-mode internal wave in a linearly stratified rectangular basin with $N = 1$ and $B = \pi^2 S^2$. (a)–(c) Vertical profiles of the vertical velocity $\tilde{w}$, horizontal velocity $\tilde{u}$ and pressure $\tilde{p}'$, respectively. (d) Time series of isopycnal displacements $\tilde{\eta} = (i\omega)^{-1}\tilde{w}$ and horizontal velocities $\tilde{u}$ induced by inviscid and dissipative modes at $z = -0.75$ with $(E/S)^{1/2} = 0.05$. (e) Time series of the first-order vertical velocity, zeroth-order pressure and first-order vertical energy flux at $z = -1$. (f) Staggered plot of vertical energy flux in time and depth. (g) Temporally averaged vertical energy flux. All variables at $x = 0.25$ are plotted.

(Note that both $+m$ and $-m$ modes must be included in the calculation.) The bottom Ekman normal velocity excites different vertical modes, including the surface wave modes, but with the same horizontal structure, as the expansion coefficients $\tilde{b}_{(l,m)(p,q)}$ are non-zero for all p but only for $q = \pm m$ in (5.4). The first-order correction to the vertical velocity is largest at the bottom and decreases towards the surface (figure 3a). The associated horizontal velocity is unidirectional, being largest in the middle of

the water column, which decreases the total (i.e. inviscid solution plus first-order correction) horizontal velocity in the upper half of the water column but increases it in the lower half (figure 3b). It also induces a phase delay to the velocity in the lower part of the water column relative to the isopycnal displacement (figure 3d). The first-order correction to the pressure decreases the total pressure except in the lower half of the water column away from the bottom (figure 3c).

The additional wave components, generated by the Ekman normal velocity, destructively interact with the parent wave and extract energy from the water column. To show this, we calculate the first-order vertical energy flux $\tilde{F}^{(1)}_{z(l,m)}$ given by

$$\tilde{F}^{(1)}_{z(l,m)} = \text{Re}\left(\tilde{p}^{(0)}_{(l,m)}e^{i\omega^{(0)}_{(l,m)}t}\right)\text{Re}\left(\tilde{w}^{(1)}_{(l,m)}e^{i\omega^{(0)}_{(l,m)}t}\right) + \text{Re}\left(\tilde{p}^{(1)}_{(l,m)}e^{i\omega^{(0)}_{(l,m)}t}\right)\text{Re}\left(\tilde{w}^{(0)}_{(l,m)}e^{i\omega^{(0)}_{(l,m)}t}\right). \quad (5.6)$$

This vertical energy flux is oscillatory and downward due to the phase lag between the pressure and vertical velocity ($=270°$; figure 3e) being locked to the parent wave. The phase between the vertical velocity and pressure changes vertically (figure 3a, c), but the vertical energy flux is net negative throughout the water column (figure 3f, g).

6. Damping of internal waves in circular basins

Rotating basin-scale internal waves in a circular basin are damped both by the internal-wave cancelling and modified spin-down. We consider a linearly stratified fluid in a flat-bottomed circular basin with radius R. Cylindrical coordinates (r, θ, z) are more appropriate for this geometry, and velocity components (u, v) are taken as the radial and azimuthal components. The celerity scale and stratification are taken as in the previous example.

The fundamental-mode Kelvin and Poincaré waves are primarily used to illustrate the damping process and its effect on the frequencies and spatial structures of the modes. These have distinct characteristics: Kelvin waves are cyclonic waves that induce strong currents near the lateral boundary, whereas super-inertial anticyclonic Poincaré waves are associated with strong currents in the middle of the basin (Csanady 1967; Antenucci & Imberger 2001; Stocker & Imberger 2003). We use the term Kelvin wave for cyclonic waves that have super-inertial frequencies because the frequency and structure changes continuously across the inertial frequency (Antenucci & Imberger 2001).

In a circular basin, all the horizontal modes, including those of basin-scale waves and geostrophic modes (Proudman 1929), need to be included in any modal expansion as in (4.17); the complete set of the modes are given in appendix B. As the horizontal modes have radial and azimuthal modes, we rewrite (l, m) and (p, q) as (l, m, n) and (p, q, n) in (4.21) and (4.22), where m and q are radial modal indices, and the common azimuthal modal index n is used below, as integrals in (4.21) with different azimuthal modal indices always vanish due to the orthogonality.

We rather arbitrarily split $\omega^{(1)}_{(l,m,n)}$ and $\tilde{b}_{(l,m,n)(p,q,n)}$ (hence $\tilde{p}'^{(1)}_{(l,m,n)}$, $\tilde{u}^{(1)}_{(l,m,n)}$ and $\tilde{v}^{(1)}_{(l,m,n)}$) such that

$$\omega^{(1)}_{(l,m,n)} = \omega^{(1)iwc}_{(l,m,n)} + \omega^{(1)sp}_{(l,m,n)} + \omega^{(1)sw}_{(l,m,n)}, \quad (6.1a)$$

$$\tilde{b}_{(l,m,n)(p,q,n)} = \tilde{b}^{iwc}_{(l,m,n)(p,q,n)} + \tilde{b}^{sp}_{(l,m,n)(p,q,n)} + \tilde{b}^{sw}_{(l,m,n)(p,q,n)}, \quad (6.1b)$$

where the first, second and third terms on the right-hand side are the first-order corrections due to $w^{iwc}_{E(l,m,n)}$, $w^{sp}_{E(l,m,n)}$ and $u^{sw}_{En(l,m,n)}$ in (4.22), respectively. Complete expressions for $\omega^{(1)}_{(l,m,n)}$ and $\tilde{b}_{(l,m,n)(p,q,n)}$ are rather lengthy and are given in appendix C.

Before discussing more general cases, we first consider the fundamental Kelvin wave mode ($m = +1$) in the high- and low-frequency limits. In order to take account of the length scale of the corner sinks and sources qualitatively, the series expansion (4.17) was terminated with the cutoff vertical wavenumber $0.5\sqrt{(E/S)^{-1}|\omega - S^{-1}|}$, corresponding to twice the thicker component of the bottom boundary layer.

In the high-frequency limit (i.e. $S^{-1} \ll \omega_{(1,+1,\pm1)}^{(0)}$), the fundamental Kelvin and Poincaré wave modes reduce to non-rotating standing internal waves (Antenucci & Imberger 2001), and both the bottom and sidewall boundary layers become Stokes layers (therefore, $\gamma_{bl} = \gamma_{sw} = \sqrt{i\omega_{(1,+1,\pm1)}^{(0)}}$ and $\gamma_{bt} = 0$). The bottom boundary layer damps the wave by the internal-wave cancelling in the same way as in rectangular basins. Damping due to the sidewall boundary layer also occurs in the same way except that the boundary-generated additional waves propagate horizontally and reflect from the sidewalls, forming a standing wave pattern horizontally. The damping rate is obtained by taking the limit $S^{-1} \ll \omega_{(1,+1,\pm1)}^{(0)}$ in (C1a, c) in appendix C:

$$\omega_{(1,\pm1,\pm1)}^{(1)} = i\sqrt{i\omega_{(1,\pm1,\pm1)}^{(0)}} \left\{ \frac{1}{2} f_{(1,1)}^V + A \frac{1}{\left(\omega_{(1,\pm1,\pm1)}^{(0)}{}^2 - 1\right)} \right\}. \qquad (6.2)$$

The first and second terms are the contributions from the internal-wave cancelling due to the bottom and sidewall boundary layers, respectively. The first term has the same form as in rectangular basins (see (5.4)), and the second term is negligible for shallow-water limit as $A \ll 1$. The result for a homogeneous water body may be recovered by setting $C = (gH)^{1/2}$, $l = 0$ and $f_{(0,0)}^V = 1$ in (6.2), and this agrees with the results previously obtained by Case & Parkinson (1957) and Mei & Liu (1973).

In the low-frequency limit (i.e. $\omega_{(1,+1,\pm1)}^{(0)} \ll S^{-1}$ provided that (3.10) is satisfied), the bottom boundary layer becomes an Ekman layer (figure 1), and the damping is the result of a process similar to spin-down (figure 4). A positive azimuthal velocity, under the Kelvin wave crest, induces a negative radial Ekman transport (figure 4b, d) towards the centre of the basin. The negative gradient of the Ekman transport causes an upward Ekman normal velocity at the bottom in addition to the sucking of the interior fluid into the bottom boundary layer by the corner sink (figure 4e). As in the spin-down problem for steady circulation, the Ekman normal velocity induces a horizontal circular flow through extension and compression of the water column (figure 4c); however, the maximum displacement is shifted by $90°$ compared to the Ekman normal velocity. As a result, the additional circular flow does not cancel the parent wave as in the spin-down, but it slants the crest and trough backwards near the wall as in low-frequency frictional Kelvin waves along a straight wall (Mofjeld 1980; Martinsen & Weber 1981; Davey, Hsieh & Wajsowicz 1983) (figure 4a–c). The downward sink flow is driven by a positive pressure, leading to a net downward radially averaged energy flux throughout the water column (figure 4f, g). This is a significant difference from the stratified spin-down of steady circulation, where diffusion is required to damp the flow in the middle of the water column (Benton & Clark 1974; Duck & Foster 2001). It is also interesting to note that the sinks and sources at the corner are responsible for draining the energy from the interior at $z = -1$; this drained energy is transported towards the centre of the basin in which part of it is returned back into the interior and the rest dissipated within the boundary layer. Although the process is not exactly the same as the spin-down of steady circulation, we use the term spin-down for the process described above in this paper.
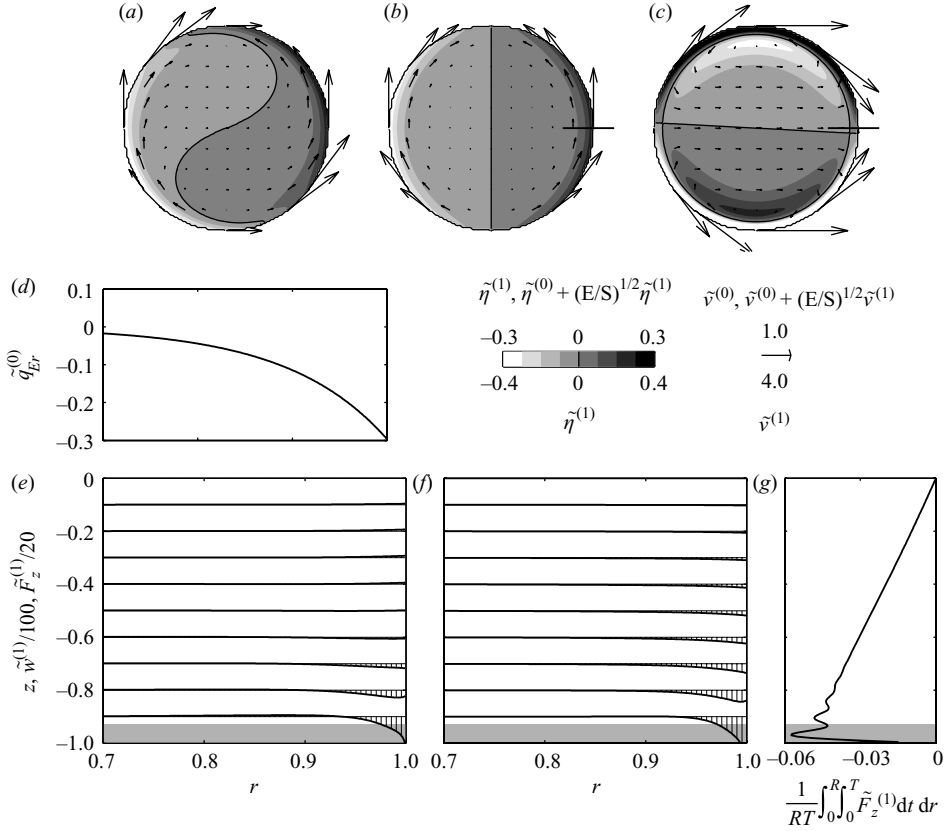
FIGURE 4. Spin-down of the fundamental internal Kelvin wave mode with $S = 0.1$ in a linearly stratified basin with $N = 1$ and $B = \pi^2 S^2$. (*a*) Plane view of the dissipative modal structure when $(E/S)^{1/2} = 0.1$. (*b*) The inviscid modal structure. (*c*) The first-order correction to the modal structure. (*d*) The radial Ekman transport along the solid line in (*b*). (*e*) Staggered plot of the first-order vertical velocity along the vertical cross-section shown in (*c*) by the solid line. (*f*) Staggered plot of the temporally averaged first-order vertical energy flux. (*g*) Temporally and radially averaged vertical energy flux. Shading and vector in (*a*)–(*c*) show the isopycnal displacements $\tilde{\eta}_{(1,+1,+1)} = (i\omega^{(0)}_{(1,+1,+1)})^{-1}\tilde{w}_{(1,+1,+1)}$ and horizontal velocities ($\tilde{u}_{(1,+1,+1)}$, $\tilde{v}_{(1,+1,+1)}$), respectively, at $z = -0.75$. The sidewall boundary layer is neglected to illustrate the spin-down process. The shaded area corresponds to twice the thickness scale of the Ekman layer. Approximately first 40 vertical modes of first 200 horizontal wave modes (including $+$ and $-$ modes) and 100 horizontal geostrophic modes are summed for plotting purposes. The solution within and slightly above the shaded area shows oscillations due to the termination of the series expansion (see the text).

The damping rate in the low-frequency limit is obtained by taking the limit $\omega^{(0)}_{(1,+1,\pm1)} \ll S^{-1}$ in (C 1*b*, *c*),

$$\omega^{(1)}_{(1,+1,\pm1)} = i f^V_{(1,1)}\sqrt{\frac{1}{2S}} \pm \frac{i\sqrt{i}}{\sqrt{\omega^{(0)}_{(1,+1,\pm1)}}}\frac{A}{S}, \qquad (6.3)$$

noting that $\gamma_{bl} = \gamma_{bt} = \sqrt{S^{-1}/2}$ in the low-frequency limit. The first and second terms are contributions from the spin-down and internal-wave cancelling due to the sidewall boundary layer, respectively. The spin-down induces damping but does not modify

the angular frequency. Neglecting the factor $f_{(1,1)}^V$, it induces damping proportional to the time scale of the spin-down, which is $\sqrt{\nu f H^{-2}}$ in a dimensional form. The damping rate due to the sidewall Ekman velocity becomes large as $\omega_{(1,+1,\pm1)}^{(0)}$ (hence S) decreases; however it is important to note that the above equation should be applied only under condition (3.10); otherwise the structure of the sidewall boundary layer deviates from the Stokes layer as discussed in §3.

The above simple limiting cases illustrate that damping of internal waves is due to a combination of the internal-wave cancelling and a modified spin-down. Interestingly, the two processes counteract for Kelvin waves. Sub-inertial Kelvin waves are damped by the spin-down part (see (6.1)) whereas the internal-wave cancelling part tends to excite the waves (figure 5e).

The roles of the two processes sharply change near $S = 0.7$, when the frequency crosses the inertial frequency (figure 5a, e). This is related to the reversal of the radial Ekman transport at the inertial frequency (figure 2); both the bottom Ekman normal velocity and the corner-source-induced flows change direction, and so does the vertical energy flux. For Poincaré waves, both mechanisms lead to wave damping. Unlike Kelvin waves, the damping rates approach zero in the low-frequency limit (figure 5f), as Poincaré wave in the limit induces small pressure variation (Antenucci & Imberger 2001), driving weak boundary-layer flows. Overall, the damping rate due to the bottom boundary layer is proportional to the corresponding angular frequencies for $S > 0.5$, but the damping rates deviate below $S \approx 0.5$ for sub- and super-inertial waves (figure 5c). The bottom Ekman normal velocity also retards both types of waves (figure 5b; note that $\omega^{(0)}$ is negative for Poincaré waves). When the Burger number is small, the sidewall boundary layer selectively damps radial mode 1 cyclonic waves (figure 5d), as they induce strong currents near the sidewall (see figure 4b).

The internal-wave cancelling and spin-down also modify the modal structure in different ways (figure 6). The modification caused by the internal-wave cancelling part due to the bottom boundary layer is negligible when the Burger number is small but becomes dominant for super-inertial waves (third column in figure 6). For super-inertial waves, it induces isopycnal displacements and velocities with a phase lag of $270°$ and $90°$ compared to the parent wave, respectively, in the lower part of the water column (figure 6s, x). This results in an intensification of the flow that delays relative to the isopycnal displacements (figure 6q, v), similar to internal waves in non-rotating rectangular basins (figure 3d).

Unlike the internal-wave cancelling, the spin-down part induces a velocity normal to the sidewall (fourth column in figure 6), and the interior fluid enters the bottom corner at $r = 1$ (see figure 4e). The circulatory flow has a $180°$ phase lag when the Burger number is small (figure 6d), but the flow becomes more unidirectional and the phase lag approaches $270°$ as the wave frequency increases to the inertial frequency (figure 6i). These modification tends to slant the crest and trough near the wall backwards (figures 4a and 6a, f), and the currents tend to be delayed relative to the isopycnal displacements. For super-inertial waves, the spin-down part induces a structure that has a relatively large amplitude and length scale smaller than the parent wave's in both the horizontal and vertical (figure 6n, t). This occurs because the temporally oscillating sinks and sources at the bottom corner may emit internal-wave rays at super-inertial frequency (Lighthill 1978; Gill 1982). As we seek oscillatory solutions with a fixed angular frequency, the rays must have a distinct angle and form a 'standing wave' pattern. Intensity of the corner sources and sinks decreases as the Burger number increases, and the fine structure eventually disappears (figure 6v, y).
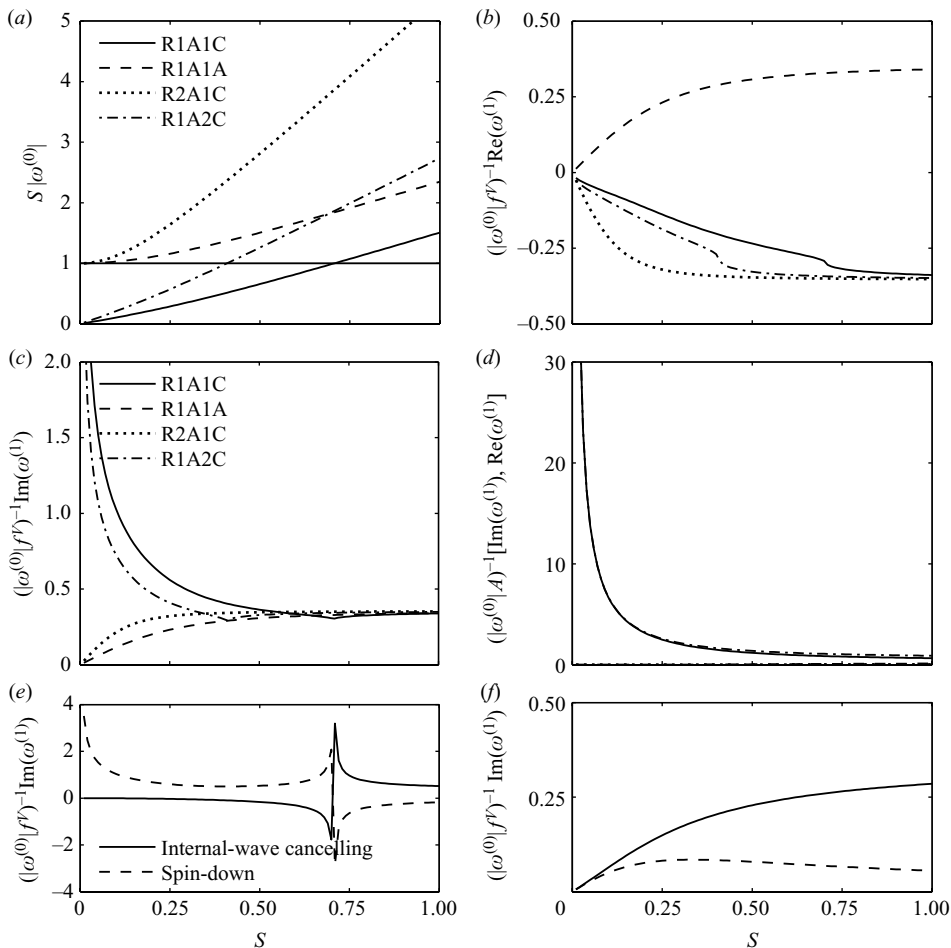
FIGURE 5. The frequency corrections and damping rates of basin-scale internal waves. (*a*) Dispersion relationships of basin-scale internal waves. (*b*), (*c*) The first-order correction to the angular frequencies and damping rates due to the bottom boundary layer, respectively. (*d*) Those due to the sidewall boundary layer (the real and imaginary parts have the same value). (*e*), (*f*) The damping rates of the fundamental Kelvin wave mode (R1A1 C) and Poincaré wave mode (R1A1 A) due to the internal-wave cancelling and spin-down, respectively. In (*d*), the dash-dotted line almost coincides with the solid line, and the dashed and dotted lines coincide with the abscissa. Note that the damping rates in (*c*) remain finite as $S \to 0$, although they appear very large due to non-normalization by $\omega^{(0)}$. Abbreviations are as follows: R indicates the radial mode number; A indicates the azimuthal mode number; C, cyclonic; and A, anti-cyclonic. For plotting purposes $\omega^{(1)}$ is divided by $f^V_{(l,l)}$ in (*b*), (*c*), (*e*) and (*f*) and by A in (*d*).

The sidewall part induces a purely radial velocity, which does not vanish at the boundary as the interior fluid enters the sidewall boundary layer (fifth column in figure 6). The velocity phase lag is 270°, relative to the leading wave for the Stokes sidewall boundary layer. The correction due to the sidewall Ekman normal velocity is small for basins with small aspect ratios.

7. Discussion

The results presented in this paper have theoretical and practical limitations. First, the sidewall-boundary-layer solution is valid only when (3.10) is satisfied.
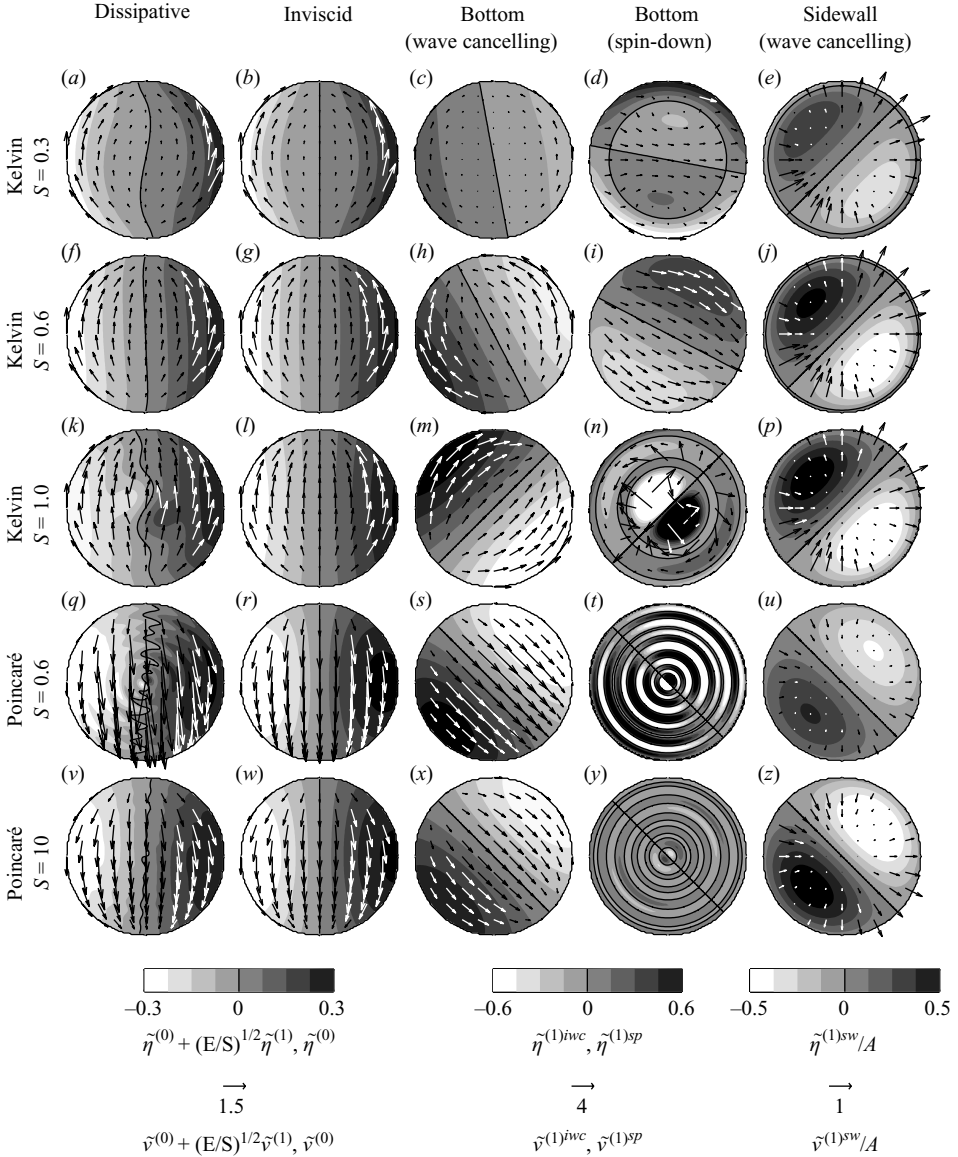
FIGURE 6. The dissipative modal structure of Kelvin waves with $S = 0.3$ (first row), $S = 0.6$ (second row) and $S = 1.0$ (third row) and that of Poincaré waves with $S = 0.6$ (fourth row) and $S = 10$ (fifth row) in linearly stratified basin with $N = 1$ and $B = \pi^2 S^2$. Shading and vector show isopycnal displacements and horizontal velocities, respectively, at $z = -0.75$. (Arrows are not shown in (*t*) and (*y*), as the directions change with a length scale shorter than the plotting interval.) The first column shows the dissipative modal structure when $(E/S)^{1/2} = 0.05$, and the second shows the inviscid modal structure. The third, fourth and fifth columns correspond to the first-order corrections by the internal-wave cancelling due to the bottom boundary layer, spin-down and internal-wave cancelling by the sidewall boundary layer, respectively. See the caption of figure 4 for number of modes used for plotting.

By introducing a shallow basin, it is also assumed that $O(A^2) \ll S^{-2} B = O(1)$ in the equation of vertical motion (3.9*e*). These conditions are not satisfied in deep basins and homogeneous basins, and the sidewall-boundary-layer solution needs

to be modified in such cases. Second, the results are not applicable when wave frequencies are very close to the inertial frequency (or $\omega \approx S^{-1}$ in (3.5)–(3.8)), as the thicker component of the bottom boundary layer becomes comparable to the total depth when $E/S \approx |\omega - S^{-1}|$ (see (3.5) and figure 1) and the corner boundary condition (3.15) becomes invalid (appendix D). Third, the first-order correction to the internal-wave field may have relatively large amplitude with smaller horizontal and vertical scales when the frequency is close to, but above, the inertial frequency. The scaling applied in the theory breaks down if the amplitude becomes so large and/or the structure becomes so fine that the nonlinear terms and/or viscosity in the interior are no longer negligible. In such a case, the inviscid solution should not be assumed as the zeroth-order solution. Fourth, the boundary layers are turbulent in reality with spatially variable turbulent viscosity, which depends on the wave amplitude in general. This modifies both magnitude and direction of the Ekman transport and induces non-exponential damping. Fifth, the assumption of a symmetric basin with a flat bottom and vertical sidewalls excludes some important processes, such as different boundary-layer structure over the sloping bottom (Thorpe 1987), existence of wave attractors in a depth-variable basin (Maas & Lam 1995) and concentration and subsequent decay of internal-wave rays due to critical-wave reflection and internal-wave refraction (Ivey & Nokes 1989; Drijfhout & Maas 2007).

An important feature of the method used in this paper is that the problem was separated into the boundary-layer flow, where viscosity enters the force balance, and the flow in the basin's interior, where viscous effects may be neglected, by introducing different length scales characteristic to each problem; the boundary-layer flow affects the interior only through the Ekman normal velocity. Strictly speaking, the same method is not applicable to real lakes, as the thickness of the bottom boundary layer is not determined by the balance between viscous force and unsteady inertia but by bottom-generated turbulence entraining the stratified fluid from the lake's interior over the stratified period (e.g. Lemckert *et al.* 2004). However, the problems are similar in the sense that dissipation plays a dominant role only in the boundary layer; turbulent flow in the well-mixed bottom boundary layer is separated from the nearly laminar interior flow by stratification suppressing turbulence at the top of the boundary layer. Therefore, we may still treat flows in lakes in the same way, considering the turbulent-boundary-layer flow and nearly inviscid interior flow communicating through the Ekman normal velocity.

Considering the above, the third limitation mentioned earlier may be overcome in real lake conditions. The well-mixed boundary layer implies that the pressure within the boundary layer is constant across the layer; so (3.2) still holds. As viscosity above the boundary layer may be neglected, a free-stress condition is more appropriate for the boundary condition at the top of the boundary layer:

$$\frac{\partial u_E}{\partial z} = \frac{\partial v_E}{\partial z} = 0 \text{ at } Z = (E/S)^{-1/2} h_{BBL}, \tag{7.1}$$

where h_{BBL} is the thickness of the mixed boundary layer in non-stretched coordinate. Assuming constant turbulent viscosity, the solution to (3.2) has the form of (3.5), but the factor $\exp(-\beta_\pm Z)$ needs to be replaced by

$$\cosh(\beta_\pm (E/S)^{-1/2}(h_{BBL} - z))/\cosh(\beta_\pm (E/S)^{-1/2} h_{BBL}), \tag{7.2}$$

and γ_{bl} and γ_{bt} given in (3.7) may be obtained by replacing $\beta_\pm$ by

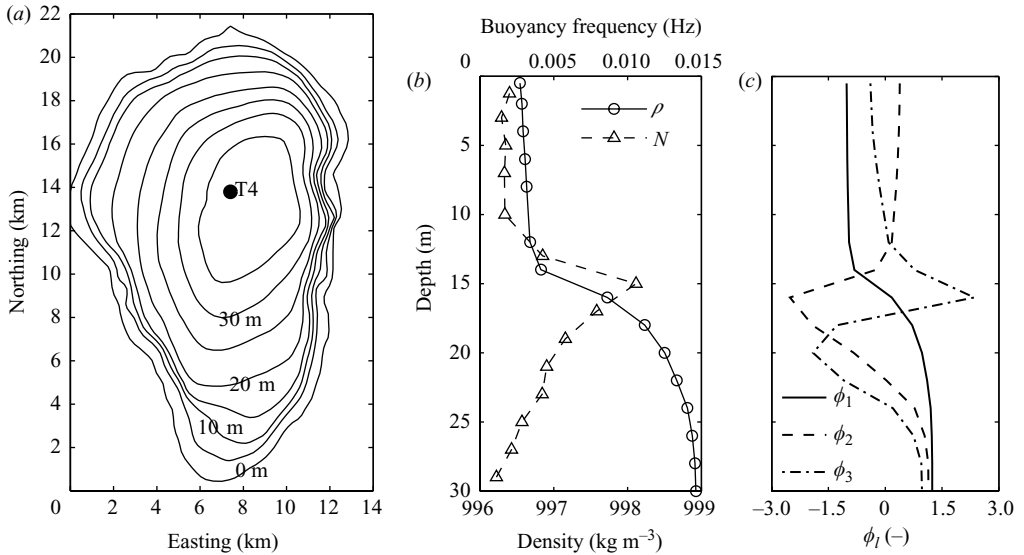$$\beta_\pm \tanh(\beta_\pm (E/S)^{-1/2} h_{BBL}). \tag{7.3}$$

FIGURE 7. Lake Kinneret: (*a*) bathymetry; (*b*) typical stratification at T4 and associated buoyancy frequency in summer; and (*c*) vertical modes under stratification in (*b*). In (*a*), the origin of the figure is situated at 32.70°N, 35.51°E, and contour lines are drawn every 5 m.

Using the new definitions of γ_{bl} and γ_{bt}, other equations apply. Although these changes are required, this does not modify the magnitude of the Ekman normal velocity significantly as long as the thickness of the thinner component of the boundary layer is thin compared to the mixed-bottom-boundary-layer thickness.

The fourth limitation may also be relaxed under some conditions. The amplitude dependence of the turbulent kinematic viscosity may be neglected if there are currents and/or waves outside of the boundary layers whose amplitudes (hence turbulence in the layers) change slowly compared to the period of the wave of interest. This also allows linear approximation of the bottom shear stress. The vertical variation of turbulent viscosity affects the Ekman transport through bottom shear stress (see (1.3)), and this effect may be captured by modifying the linear friction coefficients, γ_{bl} and γ_{bt} in (3.8) and (3.15). This requires the magnitude, phase lead and veering angle of the drag coefficient, which are well known for non-rotating boundary layers (e.g. Zou 2002) but not for capped oscillating turbulent boundary layers in a stratified rotating basin; constant turbulent viscosity may be used as a first approximation until the details become available.

It would be valuable to compare prediction of the theoretical results with the damping rates of basin-scale internal waves in Lake Kinneret. The comparison is only qualitative due to the simplified geometry used in the theory, and a comparison with laboratory experiments by Wake *et al.* (2005) was not possible because they used a relatively deep basin with two-layer stratification. Lake Kinneret is located in northern Israel with the length, width and average depth of 20 km, 10 km and 30 m, respectively (figure 7*a*). The lake is strongly stratified in summer with the thermocline located at the depth of 15–20 m, which separates the warm ($\approx 28°$C) epilimnion from the cool ($\approx 16°$C) hypolimnion (Serruya 1975). The inertial frequency is 7.8×10^{-5} rad s^{-1}, and the typical Burger number in summer is 0.6 (Antenucci & Imberger 2001). Diurnal winds in summer resonate with internal waves whose daily averaged amplitudes stays about 5 m, which appears comparable to the total depth.

High-frequency internal waves due to wind-shear-induced linear instability are observed in the lake (Boegman *et al.* 2003; Gómez-Giraldo *et al.* 2008), but they do not extract significant amount of energy from the basin-scale internal waves (Gómez-Giraldo 2007). High-frequency internal waves due to nonlinear steepening are not observed in the lake. This may be explained by the time scale for nonlinear steepening, given by (Horn, Imberger & Ivey 2001)

$$T_s = \frac{2R}{\alpha a_0}, \tag{7.4}$$

where α for vertical mode 1 internal waves is (e.g. Lamb & Yan 1996)

$$\alpha = \frac{3c_1}{2H} \frac{\int_{-H}^{0} \phi_1^3 \mathrm{d}z}{\int_{-H}^{0} \phi_1^3 \mathrm{d}z}. \tag{7.5}$$

Assuming $R = 10\,\mathrm{km}$ and $a_0 = 5\,\mathrm{m}$ and using ϕ_1 in figure 7(*c*) (but rescaled as in Lamb & Yan 1996), we get $\alpha = 5.4 \times 10^{-3}$, leading to $T_s = 9.4$ days. Since the damping times of basin-scale internal waves are a few days (Shimizu & Imberger 2008), the waves would be almost completely damped before degenerating into high-frequency waves. In fact, it is shown that linear theory explains the evolution of the basin-scale internal waves in the lake well (Shimizu & Imberger 2008); so the nonlinear effects may be neglected as a first approximation.

Use of observed turbulent viscosity within the bottom boundary layer of 10^{-4} $\mathrm{m^2\,s^{-1}}$ (Yeates & Imberger 2003) yields $E = 1.4 \times 10^{-3}$. Numerical solution of (4.7) and (4.8) under typical stratification in summer (figure 7*b*) gives the vertical modes (figure 7*c*), leading to $f_{(1,1)}^V = 1.5$ from (5.5). Using figure 5(*c*), these values yield damping rates of 2.0×10^{-6} and 4.4×10^{-6} for the horizontal mode 1 Kelvin and Poincaré waves, whose typical frequencies in summer are 7.9×10^{-5} and $17.4 \times 10^{-5}\,\mathrm{rad\,s^{-1}}$, respectively (Shimizu & Imberger 2008). The corresponding estimates from field data are 6.7×10^{-6} and $12 \times 10^{-6}\,\mathrm{rad\,s^{-1}}$, respectively; the predicted damping rates are in the same order as the estimates from field data. The result is encouraging considering that simplified geometry and constant viscosity are used in the theory. Further investigation is required to include the variation of turbulent kinematic viscosity in the boundary layers and effects of the sloping bottom, which modifies the boundary-layer dynamics (Thorpe 1987), changes the internal-wave structure (Maas & Lam 1995) and possibly introduces additional damping mechanisms (e.g. Ivey & Nokes 1989; Drijfhout & Maas 2007).

8. Conclusions

We have investigated damping rates and the dissipative modal structure of basin-scale internal waves in continuously stratified rotating circular basins. The solutions are obtained for the parameter ranges $(E/S) \ll 1$, $A \ll 1$, $EA^2 \ll S^3$ and $B = O(S^2)$ using a perturbation analysis by incorporating the Ekman normal velocities as the boundary conditions. The basin-scale internal waves are damped by a combination of the internal-wave cancelling and spin-down, which tend to counteract each other for Kelvin waves but tend to reinforce each other for Poincaré waves. In the high- and low-frequency limits, the Ekman normal velocities modify the modal structure as expected from previous studies, but when the wave frequency is of the same order as, but above, the inertial frequency, internal-wave rays emitted from the temporally oscillating sinks and sources at the bottom corner add a finer structure with a relatively

large amplitude. The damping rates predicted by the theory showed qualitatively good agreement with those estimated from field data in a strongly stratified lake.

Appendix A. Orthogonality of modes in a continuously stratified rotating basin with arbitrary shape

The orthogonality of modes in a rotating homogeneous basin was shown by Proudman (1929) and Platzman (1972), which was extended to a layer-stratified basin by Shimizu *et al.* (2007). Here, we apply a similar approach to a continuously stratified rotating basin with arbitrary shape.

Consider a continuously stratified basin with the horizontal boundary at $z = 0$ located at $(x, y) = (x_l, y_l)$ and with the bottom at $z = z_b(x, y)$, where z is the upward positive coordinate with origin at the equilibrium surface. The surface boundary condition is given by (4.3). Assuming influx of fluids at the bottom of q_b per unit plane area (e.g. due to the bottom Ekman normal velocity), the bottom boundary condition may be written as

$$-\mathrm{i}\omega \frac{S^2}{BN^2} \left(\frac{\partial p'}{\partial z}\right)_b - u_b \frac{\partial z_b}{\partial x} - v_b \frac{\partial z_b}{\partial y} = q_b \text{ at } z = z_b, \tag{A1}$$

where the vertical velocity w has been related to p' using (4.1) and the subscript b denotes a value evaluated at the bottom. If some parts of the lateral boundary are vertical, we also assume influx of q_l per unit height and unit length parallel to the boundary. Then, the lateral boundary condition is

$$u\hat{n}_x + v\hat{n}_y = -q_l \text{ at } (x, y) = (x_l, y_l). \tag{A2}$$

Let us add (A1) multiplied by $\delta(z - z_b)$ to (4.2) and write the resulting equation and (2.6c, d) in a matrix form as

$$\omega M\xi = K\xi + f_b, \tag{A3}$$

where

$$M = \begin{pmatrix} -\left(\frac{\partial}{\partial z} + \delta(z-z_b)\right)\left(\frac{S^2}{BN^2}\frac{\partial}{\partial z}\right) & 0 & 0 \\ 0 & 1 & 0 \\ 0 & 0 & 1 \end{pmatrix}, \tag{A4a}$$

$$K = \mathrm{i}\left[-\begin{pmatrix} 0 & \frac{\partial z_b}{\partial x} & \frac{\partial z_b}{\partial y} \\ 0 & 0 & 0 \\ 0 & 0 & 0 \end{pmatrix}\delta(z-z_b) + \begin{pmatrix} 0 & \frac{\partial}{\partial x} & \frac{\partial}{\partial y} \\ \frac{\partial}{\partial x} & 0 & -\frac{1}{S} \\ \frac{\partial}{\partial y} & \frac{1}{S} & 0 \end{pmatrix} \right], \tag{A4b}$$

$$f_b = -\mathrm{i}\begin{pmatrix} q_b\delta(z-z_b) \\ 0 \\ 0 \end{pmatrix} \tag{A4c}$$

are generalized version of M, K and b given by (4.5).

The matrix operators $\boldsymbol{M}$ and $\boldsymbol{K}$ in (A 3) are Hermitian (or self-adjoint), which can be shown as follows. First, multiply the left-hand side of (A 3) by the conjugate transpose of pressure and horizontal velocities that are independent of ξ, denoted with the superscript $+$ as $\bar{\boldsymbol{\xi}}^+ = (\bar{p}'^+, \bar{u}^+, \bar{v}^+)$, from the left, and integrate the expression over the basin using integration by parts. Neglecting the factor ω, using (4.1) to relate p' to w, introducing vertical displacement $\eta = (\mathrm{i}\omega)^{-1}w$ and applying the surface boundary condition (4.3), the integral may be written as

$$\int_{z_b(x)}^0 \iint \left(\boldsymbol{\xi}^{+H} \boldsymbol{M} \boldsymbol{\xi} \right) \mathrm{d}x \, \mathrm{d}y \, \mathrm{d}z$$

$$= \int_{z_b(x)}^0 \iint \left(\frac{BN^2}{S^2} \bar{\eta}^+ \eta + \bar{u}^+ u + \bar{v}^+ v \right) \mathrm{d}x \, \mathrm{d}y \, \mathrm{d}z + \iint \left(c^{(0)2} \bar{\eta}^+ \eta \right) \mathrm{d}x \, \mathrm{d}y, \quad \text{(A 5)}$$

where the superscript H stands for the conjugate transpose and the integrals in terms of x and y are taken over the basin. Using the above relation, it can be shown that

$$\int_{z_b(x)}^0 \iint \left(\boldsymbol{\xi}^{+H} \boldsymbol{M} \boldsymbol{\xi} \right) \mathrm{d}x \, \mathrm{d}y \, \mathrm{d}z = \int_{z_b(x)}^0 \iint \left[(\boldsymbol{M}\boldsymbol{\xi}^+)^H \boldsymbol{\xi} \right] \mathrm{d}x \, \mathrm{d}y \, \mathrm{d}z, \quad \text{(A 6)}$$

which means that the matrix operator on the left-hand side of (A 3) is Hermitian. Second, multiply the first term on the right-hand side of (A 3) by the conjugate transpose of $\boldsymbol{\xi}^+$ from the left and integrate over the basin using integration by parts, yielding

$$\int_{z_b(x)}^0 \iint \left(\boldsymbol{\xi}^{+H} \boldsymbol{K} \boldsymbol{\xi} \right) \mathrm{d}x \, \mathrm{d}y \, \mathrm{d}z$$

$$= -\mathrm{i} \iint \left[\bar{p}'^+_b u_b \frac{\partial z_b}{\partial x} + \bar{p}'^+_b v_b \frac{\partial z_b}{\partial y} \right] \mathrm{d}x \, \mathrm{d}y$$

$$+\mathrm{i} \int_{z_b(x)}^0 \iint \left[\frac{\partial}{\partial x}(\bar{p}'^+ u + p'\bar{u}^+) + \frac{\partial}{\partial y}(\bar{p}'^+ v + p'\bar{v}^+) \right] \mathrm{d}x \, \mathrm{d}y \, \mathrm{d}z$$

$$-\mathrm{i} \int_{z_b(x)}^0 \iint \left\{ \left[\frac{\partial \bar{p}'^+}{\partial x} u + \frac{\partial \bar{p}'^+}{\partial y} v + p' \left(\frac{\partial \bar{u}^+}{\partial x} + \frac{\partial \bar{v}^+}{\partial y} \right) \right] + \frac{1}{S}(\bar{u}^+ v - \bar{v}^+ u) \right\} \mathrm{d}x \, \mathrm{d}y \, \mathrm{d}z. \quad \text{(A 7)}$$

Further, the second term on the right-hand side can be written as

$$\mathrm{i} \oint \int_{z_b(x)}^0 \left[(\bar{p}'^+ u + p'\bar{u}^+)\hat{n}_x + (\bar{p}'^+ v + p'\bar{v}^+)\hat{n}_y \right] \mathrm{d}z \, \mathrm{d}s$$

$$+\mathrm{i} \iint \left[(\bar{p}'^+_b u_b + p'_b \bar{u}^+_b)\frac{\partial z_b}{\partial x} + (\bar{p}'^+_b v_b + p'_b \bar{v}^+_b)\frac{\partial z_b}{\partial y} \right] \mathrm{d}x \, \mathrm{d}y, \quad \text{(A 8)}$$

where $\mathrm{d}s$ is the length element along the lateral boundary and the integral in the first term on the right-hand side is taken along the basin's perimeter. Using the above relationship and (A 2), (A 7) becomes

$$\int_{z_b(x)}^0 \iint \left(\boldsymbol{\xi}^{+H} \boldsymbol{K} \boldsymbol{\xi} \right) \mathrm{d}x \, \mathrm{d}y \, \mathrm{d}z$$

$$= -\mathrm{i} \oint \int_{z_b(x)}^0 (\bar{p}'^+ q_l + p' \bar{q}^+_l) \, \mathrm{d}z \, \mathrm{d}s + \int_{z_b(x)}^0 \iint \left[(\boldsymbol{K}\boldsymbol{\xi}^+)^H \boldsymbol{\xi} \right] \mathrm{d}x \, \mathrm{d}y \, \mathrm{d}z. \quad \text{(A 9)}$$

The above equation shows that the matrix operator on the right-hand side of (A 3) is also Hermitian if $q_l = 0$, satisfying

$$\int_{z_b(\boldsymbol{x})}^0 \iint (\boldsymbol{\xi}^{+H} \boldsymbol{K} \boldsymbol{\xi}) \, \mathrm{d}x \, \mathrm{d}y \, \mathrm{d}z = \int_{z_b(\boldsymbol{x})}^0 \iint [(\boldsymbol{K}\boldsymbol{\xi}^+)^H \boldsymbol{\xi}] \, \mathrm{d}x \, \mathrm{d}y \, \mathrm{d}z. \qquad (A\,10)$$

As both the matrix operators in (A 3) are Hermitian, the homogeneous solutions of (A 3) under the conditions $q_l = q_b = 0$ (hence $\boldsymbol{f}_b = \boldsymbol{O}$) are orthogonal. The orthogonality relationships can be derived by (i) multiplying (A 3) for the rth mode by complex conjugate of modal structure of sth mode, $\bar{\tilde{\boldsymbol{\xi}}}_{(s)}$, and integrating over the basin, (ii) multiplying (A 3) for the sth mode by complex conjugate of $\tilde{\boldsymbol{\xi}}_{(r)}$ and integrating over the basin, (iii) subtracting complex conjugate of the latter equation from the former and (iv) using (A 6) and (A 10) (single modal index is used here, as the modes in basins with arbitrary geometry are not separable into different horizontal or vertical modal components in general). The result gives the orthogonal relationships

$$\int_{z_b(\boldsymbol{x})}^0 \iint \left(\tilde{\boldsymbol{\xi}}_{(s)}{}^H \boldsymbol{M} \tilde{\boldsymbol{\xi}}_{(r)}\right) \mathrm{d}x \, \mathrm{d}y \, \mathrm{d}z = \tilde{e}_{(r)} \delta_{r,s}, \qquad (A\,11a)$$

$$\int_{z_b(\boldsymbol{x})}^0 \iint \left(\tilde{\boldsymbol{\xi}}_{(s)}{}^H \boldsymbol{K} \tilde{\boldsymbol{\xi}}_{(r)}\right) \mathrm{d}x \, \mathrm{d}y \, \mathrm{d}z = \omega_{(r)} \tilde{e}_{(r)} \delta_{r,s}. \qquad (A\,11b)$$

Using (A 5), it can be seen that $\tilde{e}_{(r)}$ is twice the total energy contained in the mode. Equation (4.13) correspond to the case with $z_b = -1$.

Once orthogonality of modes (A 11) are shown, completeness of the modal expansion (4.17) can be shown by following the standard procedure (see e.g. Arfken & Weber 1995).

In the above, the orthogonality and completeness of inviscid modes in a continuously stratified basin with variable depth are derived, implicitly assuming the existence of regular modes associated with discrete natural frequencies. However, in such a basin, it is shown that regular modes may be absent, and singular eigenfunctions associated with continuous spectra may appear in the inviscid limit (e.g. Maas & Lam 1995). Further investigations are required to determine whether the theory above is extendable to eigenfunctions associated with mixed (i.e. discrete plus continuous) spectra, as in other cases (e.g. Salwen & Grosch 1981).

Appendix B. Horizontal modes in a flat-bottomed circular basin

The oscillatory solutions to (4.10) may be written as (Csanady 1967; Antenucci & Imberger 2001)

$$\eta_{w(l,m,n)} = c_l^{-1} G_{w(l,m,n)} \mathrm{e}^{-\mathrm{i}n\theta}, \qquad (B\,1a)$$

$$\begin{pmatrix} u_{w(l,m,n)} \\ v_{w(l,m,n)} \end{pmatrix} = \frac{c_l}{\omega_{(l,m,n)}^{(0)}{}^2 - S^{-2}} \left[\begin{pmatrix} \mathrm{i}\omega_{(l,m,n)}^{(0)} \\ -S^{-1} \end{pmatrix} \frac{\partial G_{w(l,m,n)}}{\partial r} + \frac{n}{r} \begin{pmatrix} -\mathrm{i}S^{-1} \\ \omega_{(l,m,n)}^{(0)} \end{pmatrix} G_{w(l,m,n)} \right] \mathrm{e}^{-\mathrm{i}n\theta},$$

$$(B\,1b)$$

where w in the superscript indicates wave modes and $G_{w(l,m,n)}(r)$ is the normalized radial function defined as

$$G_{w(l,m,n)}(r) = \frac{J_n(k_{(l,m,n)}r)}{J_n(k_{(l,m,n)})}. \qquad (B\,2)$$

In the above equations, J_n is the Bessel function of the first kind and

$$k_{(l,m,n)} = c_l^{-1} \sqrt{\left({\omega_{(l,m,n)}^{(0)}}^2 - S^{-2} \right)} \tag{B 3}$$

is the radial wavenumber (normalized by R). We use J_n throughout and let the argument be imaginary for sub-inertial waves following Stocker & Imberger (2003); for sub-inertial waves, J_n becomes the modified Bessel function of the first kind I_n by the rule $J_n(ix) = i^n I_n(x)$, where x is a real variable. The natural angular frequency $\omega_{(l,m,n)}^{(0)}$ is determined from the lateral boundary condition (Csanady 1967; Antenucci & Imberger 2001):

$$\omega_{(l,m,n)}^{(0)} \frac{\partial}{\partial r} G_{w(l,m,n)} - S^{-1} \frac{n}{r} G_{w(l,m,n)} = 0 \text{ at } r = R. \tag{B 4}$$

This gives infinite number of natural angular frequencies of different radial modes m ($\neq 0$) for given l and n. (Note that if $n > 0$, $\omega_{(l,m,n)}^{(0)} > 0$ for cyclonic waves and $\omega_{(l,m,n)}^{(0)} < 0$ for anticyclonic waves, whereas if $n < 0$, the sign of $\omega_{(l,m,n)}^{(0)}$ is opposite, guaranteeing that both $+n$ and $-n$ modes rotate in the same direction. Also note that $+n$ and $-n$ modes form the conjugate pair that satisfies (4.12).) We prefer to use $+m$ and $-m$ for cyclonic and anticyclonic waves, respectively, so that $(m, n) = (+1, \pm1)$ corresponds to the fundamental Kelvin wave mode and $(m, n) = (-1, \pm1)$ corresponds to the fundamental Poincaré wave mode. The normalization factor in (4.13a) corresponding to the choice of the radial function (B 2) is

$$\tilde{e}_{w(l,m,n)} = 2\pi \rho_{KE(l)} c_l^2 \frac{c_l^{-2} {\omega_{(l,m,n)}^{(0)}}^2 - n {\omega_{(l,m,n)}^{(0)}}^{-1} S^{-1} - n^2}{{\omega_{(l,m,n)}^{(0)}}^2 - S^{-2}}. \tag{B 5}$$

Although less attention has been paid to it, (4.10) also has steady solutions, which are necessary for completeness of the modal expansion (4.17). As seen from (4.10), any form of $\eta_{(l,m,n)}$ can be a solution when $\omega_{(l,m,n)}^{(0)} = 0$ (i.e. degenerate). One of the natural choices is the Bessel functions (Proudman 1929), and the solutions based on this choice may be written as

$$\eta_{g(l,m,n)} = \frac{S^{-1}}{\lambda_{(m,n)} c_l^2} G_{g(l,m,n)}(r) \, e^{-in\theta}, \tag{B 6a}$$

$$\begin{pmatrix} u_{g(l,m,n)} \\ v_{g(l,m,n)} \end{pmatrix} = \frac{1}{\lambda_{(m,n)}} \left\{ \begin{pmatrix} 0 \\ 1 \end{pmatrix} \frac{\partial}{\partial r} G_{g(l,m,n)}(r) \right.$$

$$\left. + \frac{n}{r} \begin{pmatrix} i \\ 0 \end{pmatrix} G_{g(l,m,n)}(r) \right\} e^{-in\theta}, \tag{B 6b}$$

where $\lambda_{(m,n)}$ are the roots of the Bessel function J_n and g in the superscript indicates geostrophic modes. The radial function may be normalized as

$$G_{g(l,m,n)}(r) = \frac{J_n(\lambda_{(m,n)} r)}{J_n(\lambda_{(m,n)})} \text{ for } n = 0, \tag{B 7a}$$

$$G_{g(l,m,n)}(r) = \frac{J_n(\lambda_{(m,n)} r)}{J_{n-1}(\lambda_{(m,n)})} \text{ for } n \neq 0. \tag{B 7b}$$

For $n \neq 0$, $\lambda_{(m,n)}$ is determined from zero-normal-velocity condition at the lateral boundary,

$$\frac{n}{r} G_{g(l,m,n)} = 0 \text{ at } r = R, \tag{B 8}$$

whereas for $n = 0$, the above condition is automatically satisfied, but $\lambda_{(m,n)}$ may be determined from the conservation of mass:

$$2\pi \int_0^R G_{g(l,m,0)}(r) \, r \, \mathrm{d}r = 0. \tag{B 9}$$

(Note that modal index m for geostrophic modes is always positive in this choice.) The normalization factor $\tilde{e}_{g(l,m,n)}$ corresponding to the choice of radial function (B 7) is

$$\tilde{e}_{g(l,m,n)} = \pi \rho_{KE(l)} \left[1 + (Sc_l \lambda_{(m,n)})^{-2} \right]. \tag{B 10}$$

As the geostrophic modes are steady, it is natural to make $\eta_{g(l,m,n)}$, $u_{g(l,m,n)}$ and $v_{g(l,m,n)}$ real by converting the factor $\mathrm{e}^{-in\theta}$ in (B 6) into cosine and sine. In this choice, n is always positive and $+m$ and $-m$ may be used for modes with cosine and sine, respectively. The conjugate pair (4.12) does not appear for steady modes in this choice as explained in the text. We merely use the form in (B 6) to simplify mathematical manipulations.

If the total mass of the basin changes, additional mode that represents spatially uniform change of $\eta_{(l,m,n)}$ is required; however, they are irrelevant for our case.

Appendix C. Expressions for $\omega^{(1)}_{(l,m,n)}$ and $\tilde{b}_{(l,m,n)(p,q,r)}$

The determination of $\omega^{(1)}_{(l,m,n)}$ and $\tilde{b}_{(l,m,n)(p,q,r)}$ is done by rewriting (l, m) and (p, q) as (l, m, n) and (p, q, r), respectively, in (4.21), substituting (B 1) and (B 6) into the equation and performing the integrations. Separating as $\omega^{(1)}_{(l,m,n)}$ in (6.1a), the angular frequencies are given by

$$\frac{\omega^{(1)iwc}_{(l,m,n)}}{\omega^{(0)}_{(l,m,n)}} = \frac{f^V_{(l,l)} f^{iwc}_{(l,m,n)}}{f^{w,E}_{(l,m,n)}} \left[\frac{1}{2} \left(\omega^{(0)\,2}_{(l,m,n)} - n^2 \right) \right], \tag{C 1a}$$

$$\frac{\omega^{(1)sp}_{(l,m,n)}}{\omega^{(0)}_{(l,m,n)}} = -\mathrm{i} \frac{f^V_{(l,l)} f^{sp}_{(l,m,n)}}{f^{w,E}_{(l,m,n)}} \left[n - \frac{1}{2} \frac{S^{-1}}{\omega^{(0)}_{(l,m,n)}} \left(\omega^{(0)\,2}_{(l,m,n)} - n^2 \right) \right], \tag{C 1b}$$

$$\frac{\omega^{(1)sw}_{(l,m,n)}}{\omega^{(0)}_{(l,m,n)}} = A \frac{f^{sw}_{(l,m,n)}}{f^{w,E}_{(l,m,n)}} [n^2], \tag{C 1c}$$

where $f^V_{(l,l)}$ is defined by (5.5) and

$$f^{iwc}_{(l,m,n)} = \frac{\mathrm{i}\omega^{(0)}_{(l,m,n)} \gamma_{bl} + S^{-1} \gamma_{bt}}{\omega^{(0)\,2}_{(l,m,n)} - S^{-2}}, \tag{C 2a}$$

$$f^{sp}_{(l,m,n)} = \frac{S^{-1} \gamma_{bl} - \mathrm{i}\omega^{(0)}_{(l,m,n)} \gamma_{bt}}{\omega^{(0)\,2}_{(l,m,n)} - S^{-2}}, \tag{C 2b}$$

$$f^{sw}_{(l,m,n)} = \frac{\mathrm{i}\gamma_{sw}}{\omega^{(0)}_{(l,m,n)}}, \tag{C 2c}$$

$$f^{w,E}_{(l,m,n)} = \frac{\omega^{(0)\,2}_{(l,m,n)}}{\omega^{(0)\,2}_{(l,m,n)} - S^{-2}} \left(\frac{\omega^{(0)\,2}_{(l,m,n)}}{c_l^2} - \frac{n}{S\omega^{(0)}_{(l,m,n)}} - n^2 \right). \tag{C 3}$$

The expansion coefficients $\tilde{b}_{(l,m,n)(p,q,r)}$ need to be calculated separately for the wave modes and geostrophic modes with $n=0$ and $n\neq 0$. For the wave modes, we get

$$\tilde{b}^{w,iwc}_{(l,m,n)(p,q,r)} = \frac{f^{V}_{(l,p)}f^{iwc}_{(l,m,n)}}{f^{w,E}_{(p,q,r)}}\frac{\omega^{(0)}_{(l,m,n)}}{\omega^{(0)}_{(l,m,n)}-\omega^{(0)}_{(p,q,r)}}$$
$$\times\left[f^{w,I}_{(l,m,n)(p,q,r)}\left(\frac{S^{-1}}{\omega^{(0)}_{(l,m,n)}}-\frac{S^{-1}}{\omega^{(0)}_{(p,q,r)}}\right)\right]\delta_{r,n}, \quad (C\,4a)$$

$$\tilde{b}^{w,sp}_{(l,m,n)(p,q,r)} = -i\frac{f^{V}_{(l,p)}f^{sp}_{(l,m,n)}}{f^{w,E}_{(p,q,r)}}\frac{\omega^{(0)}_{(l,m,n)}}{\omega^{(0)}_{(l,m,n)}-\omega^{(0)}_{(p,q,r)}}$$
$$\times\left[n\frac{\omega^{(0)\,2}_{(p,q,r)}}{c_l^2\omega^{(0)\,2}_{(l,m,n)}}-\frac{f^{w,I}_{(l,m,n)(p,q,r)}S^{-1}}{\omega^{(0)}_{(l,m,n)}}\left(\frac{S^{-1}}{\omega^{(0)}_{(l,m,n)}}-\frac{S^{-1}}{\omega^{(0)}_{(p,q,r)}}\right)\right]\delta_{r,n}, \quad (C\,4b)$$

$$\tilde{b}^{w,sw}_{(l,m,n)(p,q,r)} = \frac{Af^{sw}_{(l,m,n)}}{f^{w,E}_{(p,q,r)}}\frac{\omega^{(0)}_{(l,m,n)}}{\omega^{(0)}_{(l,m,n)}-\omega^{(0)}_{(p,q,r)}}\left[n^2\frac{\omega^{(0)\,2}_{(p,q,r)}}{\omega^{(0)\,2}_{(l,m,n)}}\right]\delta_{l,p}\delta_{r,n}, \quad (C\,4c)$$

where

$$f^{w,I}_{(l,m,n)(p,q,r)} = \frac{\omega^{(0)\,2}_{(p,q,r)}}{\omega^{(0)\,2}_{(p,q,r)}-S^{-2}}\frac{k_{(p,q,r)}^{2}}{k_{(p,q,r)}^{2}-k_{(l,m,n)}^{2}}. \quad (C\,5)$$

For the geostrophic modes with $n=0$, we get

$$\tilde{b}^{g,iwc}_{(l,m,n)(p,q,r)} = \frac{f^{V}_{(l,p)}f^{iwc}_{(l,m,n)}}{f^{g,E}_{(p,q,r)}}\left[2f^{g,I}_{(l,m,n)(p,q,r)}\frac{1}{\lambda_{(q,r)}}\frac{\omega^{(0)}_{(l,m,n)}+S^{-1}}{\omega^{(0)}_{(l,m,n)}}\right]\delta_{r,n}, \quad (C\,6a)$$

$$\tilde{b}^{g,sp}_{(l,m,n)(p,q,r)} = -i\frac{f^{V}_{(l,p)}f^{sp}_{(l,m,n)}}{f^{g,E}_{(p,q,r)}}$$
$$\times\left[2n\frac{S^{-1}}{c_p\lambda_{(q,r)}\omega^{(0)\,2}_{(l,m,n)}}-2\frac{f^{g,I}_{(l,m,n)(p,q,r)}S^{-1}}{\omega^{(0)}_{(l,m,n)}\lambda_{(q,r)}}\frac{\omega^{(0)}_{(l,m,n)}+S^{-1}}{\omega^{(0)}_{(l,m,n)}}\right]\delta_{r,n}, \quad (C\,6b)$$

$$\tilde{b}^{g,sw}_{(l,m,n)(p,q,r)} = \frac{Af^{sw}_{(l,m,n)}}{f^{g,E}_{(p,q,r)}}\left[2n^2\frac{S^{-1}}{\omega^{(0)\,2}_{(l,m,n)}\lambda_{(q,r)}}\right]\delta_{p,l}\delta_{r,n}, \quad (C\,6c)$$

where

$$f^{g,E}_{(l,m,n)} = 1+\frac{S^{-2}}{c_l^2\lambda_{(m,n)}^{2}}, \quad (C\,7)$$

$$f^{g,I}_{(l,m,n)(p,q,r)} = \frac{S^{-1}}{c_p}\frac{1}{\lambda_{(q,r)}^{2}-\left(\omega^{(0)\,2}_{(l,m,n)}-S^{-2}\right)}. \quad (C\,8)$$

For geostrophic modes with $n\neq 0$, the results are

$$\tilde{b}^{g,iwc}_{(l,m,n)(p,q,r)} = -\frac{f^{V}_{(l,p)}f^{iwc}_{(l,m,n)}}{f^{g,E}_{(p,q,r)}}\left[2f^{g,I}_{(l,m,n)(p,q,r)}\right]\delta_{r,n}, \quad (C\,9a)$$

$$\tilde{b}^{g,sp}_{(l,m,n)(p,q,r)} = i\frac{f^{V}_{(l,p)}f^{sp}_{(l,m,n)}}{f^{g,E}_{(p,q,r)}}\left[0-2\frac{S^{-1}}{\omega^{(0)}_{(l,m,n)}}f^{g,I}_{(l,m,n)(p,q,r)}\right], \quad (C\,9b)$$

$$\tilde{b}^{g,sw}_{(l,m,n)(p,q,r)} = 0. \quad (C\,9c)$$

The first and second terms in (C 1b), (C 4b), (C 6b) and (C 9b) correspond to the corner jet at $r = 1$ and the Ekman normal velocity for $r < 1$, respectively.

Appendix D. Flow field around the corner region

This appendix aims to show validity of the corner boundary condition (3.15) in the limit of small viscosity by numerically investigating detailed flow field around the bottom-corner region of a flat-bottomed circular basin filled with a viscous fluid.

Numerical solutions of the fundamental-mode internal Kelvin and Poincaré waves are obtained neglecting non-hydrostatic effects and diffusion of density, to be consistent with the scaling used in the analytical investigation. The governing equations for a monochromatic wave with an angular frequency ω may be written as

$$\omega M \xi = (K + D) \xi, \tag{D 1}$$

where the scaling in §2 is applied with $L = R$, $\omega_0 = C/R$ and $S = C(fR)^{-1}$ (as in §6). The variables ξ, M and K are defined by (4.5) with $w_E = 0$, and the viscous operator D is defined as

$$D = -\mathrm{i}\frac{E}{S}\begin{pmatrix} 0 & 0 & 0 \\ 0 & \nabla^2 & 0 \\ 0 & 0 & \nabla^2 \end{pmatrix}, \tag{D 2}$$

where the horizontal derivatives in the Laplacian is retained to resolve the sidewall boundary layers. The no-slip boundary condition is applied at the bottom and sidewalls. Assuming azimuthal mode 1 waves, we set $\xi(r, \theta, z) = \xi(r, z)\mathrm{e}^{-\mathrm{i}\theta}$ and $C = c_1$. Equation (D 1) is discretized in the r–z plane using the control volume method with a staggard grid (Patankar 1980). Depending on the boundary-layer thicknesses, $80 \sim 120$ and $50 \sim 100$ computational cells are used in the radial and vertical directions, respectively. The height and width of the cells are increased exponentially from the bottom and sidewalls, respectively, in order to resolve the boundary layers with at least 15 cells. Homogeneous solutions to (D 1) are obtained by numerically solving the resulting matrix equation as an eigenvalue problem. Vertical velocities are calculated diagnostically from the solutions using (4.1).

The flow field around the corner region under the fundamental-mode sub-inertial internal Kelvin wave is shown in figure 8(a). The phase corresponds to $\omega t - \theta \approx 0$ in the analytical solution (B 1); so both radial and vertical velocities would be zero everywhere in the inviscid limit. (The azimuthal velocity above the bottom boundary layer is into the paper.) In particular, note that the currents in the bottom boundary layer (below the dotted line in figure 8a) are due to the Ekman transport and that the sidewall boundary layers are about 100 times thinner than the bottom boundary layer since $A = 0.01$. The Ekman transport is clearly fed by the sink flow in the corner region, as discussed in §3.3. The width and height of the corner region may be conveniently defined by a point at which $u = w = 0$ (filled circle in figure 8a). The height decreases as $\sim (E/S)^{1/2}$ (figure 8d), as indicated by the scaling for the bottom-boundary-layer thickness in §3.1. The width follows $(E/S)^{-a}$ for small E/S, where a decreases with increasing S ($a = 0.34, 0.26, 0.17$ for $S = 0.1, 0.3, 0.6$, respectively; note that the flow regime changes above $S > 0.7$ as the Kelvin wave becomes super-inertial). The aspect ratio of the basin, A, does not affect the height and width. Therefore, the corner region becomes infinitely small in the limit $E/S \to 0$, and (3.15) provides an adequate corner boundary condition.

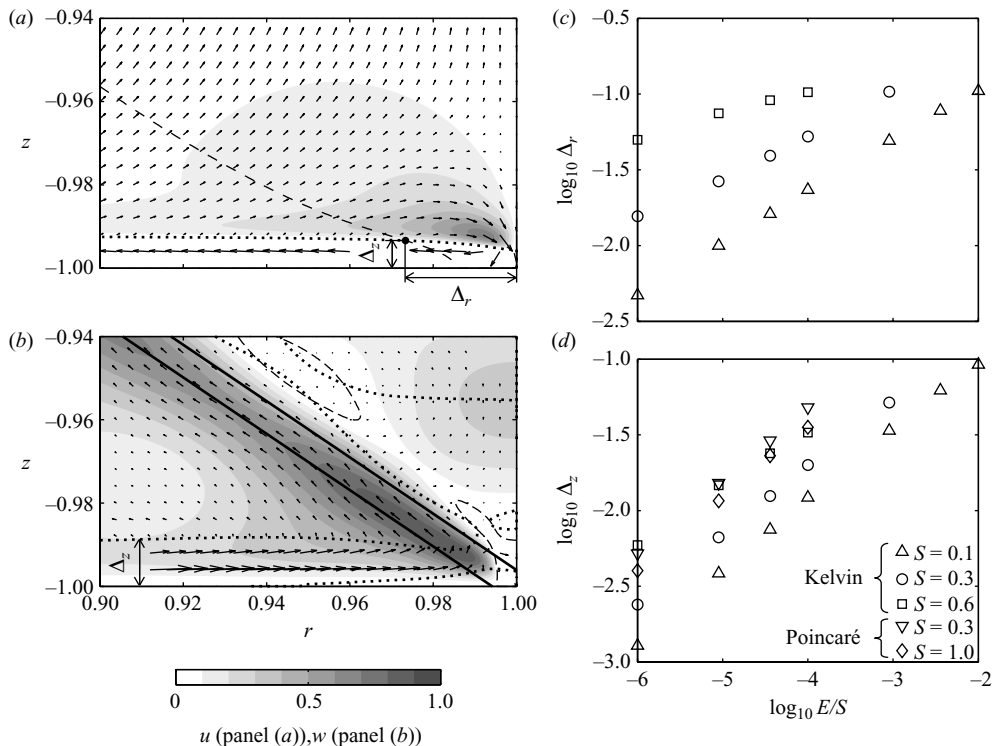FIGURE 8. The bottom-corner region in a circular basin with $A = 0.01$. Flow field under the fundamental-mode internal (*a*) Kelvin wave with $E/S = 3 \times 10^{-3}$ and $S = 0.3$ and (*b*) Poincaré wave with $E/S = 3 \times 10^{-3}$ and $S = 1.0$. The phase corresponds to $\omega t - \theta \approx 0$ in the analytical solution (B 1), so that both the radial and vertical velocities would be zero everywhere in the inviscid limit. (The azimuthal velocities above the bottom boundary layer are into and out of the paper in (*a*) and (*b*), respectively.) Arrows show normalized velocity, and the dotted and dashed lines show contour lines for $u = 0$ and $w = 0$, respectively. Shading illustrates the area strongly influenced by the corner jets (horizontal and vertical velocities in (*a*) and (*b*), respectively). The thick solid lines indicate the angle of internal-wave ray, calculated from (D 3), with the vertical distance corresponding to the bottom-boundary-layer thickness. (*c*) The width and (*d*) height of the corner region, defined as in (*a*) and (*b*). The width is not calculated for Poincaré waves due to difficulty in objectively determining the value from numerical results.

The flow field under the fundamental-mode super-inertial internal Poincaré wave is shown in figure 8(*b*). The phase again corresponds to $\omega t - \theta \approx 0$, and the azimuthal velocity above the bottom boundary layer is out of the paper. The Ekman transport leaves the bottom boundary layer in the corner region, forming internal-wave rays (figure 8*b*) with an angle (Gill 1982)

$$\theta_r = \tan^{-1} \left(\frac{\omega^2 - S^{-2}}{BN^2 S^{-2} A^{-2} - \omega^2} \right) \tag{D 3}$$

in the scaled coordinates. It should be noted that the rays become obscure with increasing E/S, since the currents induced by the rays are relatively insensitive to E/S (note that both the flow rate out of the corner region and the ray thickness are proportional to $[E/S]^{1/2}$) and the Ekman normal velocity increases as $\sim (E/S)^{1/2}$. It is not easy to separate the flows induced by the Ekman normal velocity and the

corner region in the numerical solutions objectively; however, it is physically required that the width is $\theta_r^{-1}\Delta_z'$, where Δ_z' is the ray height. Since Δ_z' scales with the bottom-boundary-layer height that decreases as $\sim(E/S)^{1/2}$ (figure 8d), (3.15) provides a corner boundary condition in the limit $E/S \to 0$ unless $\theta_r \ll 1$ (i.e. the wave frequency is very close to the inertial frequency).

REFERENCES

ANTENUCCI, J. P. & IMBERGER, J. 2001 Energetics of long internal gravity waves in large lakes. *Limnol. Oceanogr.* **46**, 1760–1773.

ARFKEN, G. B. & WEBER, H. J. 1995 *Mathematical Methods for Physicists*, 4th edn. Academic.

BARCILON, V. & PEDLOSKY, J. 1967*a* Linear theory of rotating stratified fluid motions. *J. Fluid Mech.* **29**, 1–16.

BARCILON, V. & PEDLOSKY, J. 1967*b* A unified theory of homogeneous and stratified rotating fluid. *J. Fluid Mech.* **29**, 609–621.

BENTON, E. R. & CLARK, A., JR. 1974 Spin-up. *Annu. Rev. Fluid Mech.* **6**, 257–280.

BOEGMAN, L., IMBERGER, J., IVEY, G. N. & ANTENUCCI, J. P. 2003 High-frequency internal waves in large stratified lakes. *Limnol. Oceanogr.* **45**, 895–919.

BRINK, K. H. 1982 The effect of bottom friction on low-frequency coastal trapped waves. *J. Phys. Oceanogr.* **12**, 127–133.

BRINK, K. H. 1988 On the effect of bottom friction on internal waves. *Cont. Shelf Res.* **8**, 397–403.

BRINK, K. H. & ALLEN, J. S. 1978 On the effect of bottom friction on barotropic motion over the continental shelf. *J. Phys. Oceanogr.* **8**, 919–922.

CASE, K. M. & PARKINSON, W. C. 1957 Damping of surface waves in an incompressible liquid. *J. Fluid Mech.* **2**, 172–184.

CLARKE, A. J. & VAN GORDER, S. 1986 A method for estimating wind-driven frictional, time-dependent, stratified shelf and slope water flow. *J. Phys. Oceanogr.* **16**, 1013–1028.

CSANADY, G. T. 1967 Large-scale motion in the Great Lakes. *J. Geophys. Res.* **72**, 4151–4162.

DAVEY, M. K., HSIEH, W. W. & WAJSOWICZ, R. C. 1983 The free Kelvin wave with lateral and vertical viscosity. *J. Phys. Oceanogr.* **13**, 2182–2191.

DEFANT, A. 1961 *Physical Oceanography*, vol. II. Pergamon.

DINTRANS, B., RIEUTORD, M. & VALDETTARO, L. 1999 Gravito-inertial waves in a rotating stratified sphere or spherical shell. *J. Fluid Mech.* **398**, 271–297.

DORE, B. D. 1968 The viscous damping of internal waves on the rotating earth. *Pure Appl. Geophys.* **71**, 118–131.

VAN DORN, W. G. 1966 Boundary dissipation of oscillatory waves. *J. Fluid Mech.* **24**, 769–779.

DRIJFHOUT, S. & MAAS, L. R. M. 2007 Impact of channel geometry and rotation on the trapping of internal tides. *J. Phys. Oceanogr.* **37**, 2740–2763.

DUCK, P. W. & FOSTER, M. R. 2001 Spin-up of homogeneous and stratified fluid. *Annu. Rev. Fluid Mech.* **33**, 231–263.

VAN DYKE, M. 1964 *Perturbation Methods in Fluid Mechanics*. Academic.

GILL, A. E. 1982 *Atmosphere–Ocean Dynamics*. Academic.

GÓMEZ-GIRALDO, E. A. 2007 Observation of energy transfer mechanisms associated with internal waves. PhD Thesis. University of Western Australia.

GÓMEZ-GIRALDO, A., IMBERGER, J., ANTENUCCI, J. P. & YEATES, P. S. 2008 Wind-shear-generated high-frequency internal waves as precursors to mixing in a stratified lake. *Limnol. Oceanogr.* **53**, 354–367.

GREENSPAN, H. P. 1968 *Theory of Rotating Fluid*. Cambridge University Press.

HODGES, B. R., IMBERGER, J., SAGGIO, A. & WINTERS, K. B. 2000 Modeling basin-scale internal waves in a stratified lake. *Limnol. Oceanogr.* **45**, 1603–1620.

HORN, D. A., IMBERGER, J. & IVEY, G. N. 2001 The degeneration of large-scale interfacial gravity waves in lakes. *J. Fluid Mech.* **434**, 181–207.

HUNT, J. N. 1952 Viscous damping of waves over an inclined bed in a channel with finite width. *Houille Blanche* **7**, 836–842.

HURLEY, D. G. & IMBERGER, J. 1969. Surface and internal waves in a liquid of variable depth. *Bull. Aust. Math. Soc.* **1**, 29–46.

IVEY, G. N. & NOKES, R. I. 1989 Vertical mixing due to the breaking of critical internal waves on sloping boundaries. *J. Fluid Mech.* **204**, 479–500.

JOHNS, B. 1968 A boundary layer method for the determination of the viscous damping of small amplitude gravity waves. *Quart. J. Mech. Appl. Math.* **21**, 93–103.

KALABA, R., SPINGARN, K. & TESFATSION, L. 1981 Variational equations for the eigenvalues and eigenvectors of nonsymmetric matrices. *J. Optim. Theory App.* **33**, 1–8.

LAMB, H. 1932 *Hydrodynamics*, 6th edn. Dover.

LAMB, K. G. & YAN, L. 1996 The evolution of internal wave undular bores: comparisons with a fully nonlinear numerical model with weakly nonlinear theory. *J. Phys. Oceanogr.* **26**, 2712–2734.

LEBLOND, P. H. 1966 On the damping of internal gravity waves in a continuously stratified ocean. *J. Fluid Mech.* **25**, 121–142.

LEMCKERT, C., ANTENUCCI, J., SAGGIO, A. & IMBERGER, J. 2004 Physical properties of turbulent benthic boundary layers generated by internal waves. *J. Hydraul. Engng* **130**, 58–69.

LIGHTHILL, J. 1978. *Waves in Fluids*. Cambridge University Press.

MAAS, L. R. M. & LAM, F.-P. A. 1995 Geometric focusing of internal waves. *J. Fluid Mech.* **300**, 1–41.

MARTINSEN, E. A. & WEBER, J. E. 1981 Frictional influence on internal Kelvin waves. *Tellus* **33**, 402–410.

MEI, C. C. & LIU, L. F. 1973 The damping of surface gravity waves in a bounded liquid. *J. Fluid Mech.* **59**, 239–256.

MITSUDERA, H. & HANAWA, K. 1988 Damping of coastal trapped waves due to bottom friction in a baroclinic ocean. *Cont. Shelf Res.* **8**, 113–129.

MOFJELD, H. O. 1980 Effects of vertical viscosity on Kelvin waves. *J. Phys. Oceanogr.* **10**, 1039–1050.

PATANKAR, S. V. 1980 *Numerical Heat Transfer and Fluid Flow*. Hemisphere.

PEDLOSKY, J. 1979 *Geophysical Fluid Dynamics*. Springer.

PLATZMAN, G. W. 1972 Two-dimensional free oscillations in natural basins. *J. Phys. Oceanogr.* **2**, 117–138.

PLATZMAN, G. W. 1984 Normal modes of the World Ocean. Part 3. A procedure for tidal synthesis. *J. Phys. Oceanogr.* **14**, 1521–1531.

PROUDMAN, J. 1929 On a general expansion in the theory of the tides. *Proc. Lond. Math. Soc.* **29**, 527–536.

ROMEA, R. D. & ALLEN, J. S. 1984 The effect of friction and topography on coastal internal Kelvin waves at low latitude. *Tellus* **36A**, 384–400.

SAGGIO, A. & IMBERGER, J. 2001 Mixing and turbulent fluxes in the metalimnion of a stratified lake. *Limnol. Oceanogr.* **46**, 392–409.

SALWEN, H. & GROSCH, C. E. 1981 The continuous spectrum of the Orr–Sommerfeld equation. Part 2. Eigenfunction expansions. *J. Fluid Mech.* **104**, 445–465.

SERRUYA, S. 1975 Wind, water temperature and motions in Lake Kinneret: general pattern. *Verh. Intl Verein. Limnol.* **19**, 73–87.

SHIMIZU, K. & IMBERGER, J. 2008 Energetics and damping of internal waves in a strongly stratified lake. *Limnol. Oceanogr.* **53**, 1574–1588.

SHIMIZU, K., IMBERGER, J. & KUMAGAI, M. 2007 Horizontal structure and excitation of primary motions in a strongly stratified lake. *Limnol. Oceanogr.* **52**, 2641–2655.

SPENCE, G. S. M., FOSTER, M. R. & DAVIS, P. A. 1992 The transient response of a contained rotating stratified fluid to impulsively started surface forcing. *J. Fluid Mech.* **243**, 33–50.

STEWARTSON, K. 1957 On almost rigid rotations. *J. Fluid Mech.* **3**, 17–26.

STOCKER, R. & IMBERGER, J. 2003 Energy partitioning and horizontal dispersion in a stratified rotating lake. *J. Phys. Oceanogr.* **33**, 512–529.

THORPE, S. A. 1987 Current and temperature variability on the continental slope. *Phil. Trans. R. Soc. Lond.* A **323**, 471–517.

URSELL, F. 1952 Edge waves on a sloping beach. *Proc. R. Soc. Lond.* A **214**, 79–97.

WAKE, G. W., IVEY, G. N. & IMBERGER, J. 2005 The temporal evolution of baroclinic basin-scale waves in a rotating circular basin. *J. Fluid Mech.* **523**, 367–392.

WALIN, G. 1969 Some aspects of time-dependent motion of a stratified rotating fluid. *J. Fluid Mech.* **36**, 289–307.

WÜEST, A., PIEPKE, G. & VAN SENDEN, D. C. 2000 Turbulent kinetic energy balance as a tool for estimating vertical diffusivity in wind-forced stratified waters. *Limnol. Oceanogr.* **45**, 1388–1400.

YEATES, Y. & IMBERGER, J. 2003 Pseudo two-dimensional simulations of internal and buoyancy fluxes in stratified lakes and reservoirs. *Intl J. River Basin Manage.* **1**, 297–319.

ZOU, Q. 2002 An analytical model of wave bottom boundary layers incorporating turbulent relaxation and diffusion effects. *J. Phys. Oceanogr.* **32**, 2441–2456.